A Modular Energy Aware Framework for Multicopter Modeling in Control and Planning Applications

Sebastian Gasche, Christian Kallies, Andreas Himmel, and Rolf Findeisen

***Abstract*—Unmanned aerial vehicles (UAVs), especially multicopters, have recently gained popularity for use in surveillance, monitoring, inspection, and search and rescue missions. Their maneuverability and ability to operate in confined spaces make them particularly useful in cluttered environments. For advanced control and mission planning applications, accurate and resource-efficient modeling of UAVs and their capabilities is essential. This study presents a modular approach to multicopter modeling that considers vehicle dynamics, energy consumption, and sensor integration. The power train model includes detailed descriptions of key components such as the lithium-ion battery, electronic speed controllers, and brushless DC motors. Their models are validated with real test flight data. In addition, sensor models, including LiDAR and cameras, are integrated to describe the equipment often used in surveillance and monitoring missions. The individual models are combined into an energy-aware multicopter model, which provide the basis for a companion study on path planning for unmanned aircaft system (UAS) swarms performing search and rescue missions in cluttered and dynamic environments. The flexible modeling approach enables easy description of different UAVs in a heterogeneous UAS swarm, allowing for energy-efficient operations and autonomous decision making for a reliable mission performance.**

***Index Terms*—unmanned aerial vehicle, unmanned aircraft system, multicopter, energy consumption, modular modeling**

I. Introduction

Today, unmanned aerial vehicles (UAVs) are used in various industrial and civilian applications, including search and rescue, surveillance, and inspection missions, due to their flexibility, ease of deployment, and ability to access hard-to-reach areas. They are available in a wide range of designs, such as fixed-wing, rotary-wing, and hybrid configurations, each suited to specific mission profiles [36]. Among them, multicopters are notable for their high maneuverability, stability, and ability to hover, making them particularly effective in cluttered environments such as urban, forested, or disaster-affected areas. Motivated by their suitability for tasks in confined and complex environments where other types of UAVs may struggle, this study focuses on multicopters [26].

Many tasks such as mission planning, path planning, control, and state estimation require accurate models of the UAV's dynamics to ensure that the UAV performs as expected. This includes the UAV's vehicle dynamics, such as forces and moments acting on the body, as well as rotational and translational motions. In addition, its interaction with the environment, including disturbances such as wind or turbulence, must also be taken into account. Besides the vehicle dynamics, the dynamics of its energy consumption is often important to model. As the energy consumption has a direct influence on the flight time, an accurate modeling enables to realistically estimate the flight endurance and the mission feasibility.

These models are central to several control and optimization methods, such as model predictive control (MPC), which require accurate models of the system to predict future states and adjust controls accordingly [24, 35, 43]. For instance, in our companion study [14] on path planning for a heterogeneous unmanned aircraft system (UAS) swarm with the goal of planning flight paths for search and rescue missions, models of the UAVs' vehicle dynamics and energy consumption are used. The path planning algorithm is based on MPC and mixed integer linear programming (MILP), which means that a mathematical model of the vehicle, the environment, and the mission goal is needed for path planning and decision making. Based on these models, the future behavior of the UASs is predicted and optimized in terms of mission success, energy efficiency, and safety, enabling cooperative and sustainable swarm guidance. Furthermore, the estimation of the remaining energy capacity of the UAVs, which is integrated into the decision making, enables the autonomous return of discharged UAVs to their landing sites for recharging. Other path planning algorithms, such as rapidly-exploring random trees [19, 20] and genetic algorithms [23, 33], also benefit from such models to incorporate motion constraints during sampling.

Sensors, such as cameras and LIDARs, which are common payloads for UAS missions, also impose constraints on UAS operations to ensure valid data collection. Therefore, the effects of the sensors on the dynamics and energy consumption of the UAV should be considered for accurate planning tasks.

In modeling, there are three primary types of models that differ in required knowledge of the inner dynamics of the system, required data on the system response, and descriptiveness. *White-box models*, also known as physics-based or first-principles models, analytically model system behavior based on physical equations where all parameters must be known. While highly interpretable and providing detailed insight into underlying physics, they require precise knowledge of all system components, challenging for complex systems. They offer high accuracy when the system is well understood but can be computationally expensive, limiting their use in real-time applications. *Black-box models* rely purely on input-output

S. Gasche and C. Kallies are with the Institute of Flight Guidance, German Aerospace Center, Brunswick, Germany.

S. Gasche, A. Himmel and R. Findeisen are with the Technical University of Darmstadt, Darmstadt, Germany.

data without requiring detailed understanding of inner system dynamics. These models use machine learning or system identification methods to model system behavior as a relation between input and output. They can capture complex nonlinear system dynamics and are easy to implement with large datasets but lack physical interpretability. Additionally, their limited extrapolation capabilities result in inaccuracies when encountering unlearned situations, as accuracy depends on training data quantity and quality. *Grey-box models* combine elements of white-box and black-box models, using partial knowledge of inner dynamics while estimating unknown parameters or component dynamics from data. This offers a balance between accuracy and computational efficiency, particularly useful in practical applications, where some system knowledge is available but precise modeling of every component or process is impractical. However, determining the optimal model structure can be challenging, requiring both physical knowledge and data [2, 41].

In this study, a grey-box modeling approach is used for its balance of accuracy, flexibility, and computational efficiency. It allows the incorporation of known UAV dynamics [7, 13, 31, 40], the approximation of difficult-to-model dynamics, and the consideration of uncertain or unknown parameters. In addition, we are aiming at a modular model for multicopters, which offers significant advantages in terms of flexibility and configurability. Multicopters can vary widely in the number of rotors, payloads, sensors, and battery capacities. A modular approach allows components such as motors, propellers, batteries and sensors to be easily reconfigured or replaced without overhauling the entire model. This is particularly useful when planning missions where the UAV may need to be configured to perform different tasks or operate in different environments. For example, by swapping out modules such as batteries or motors, the model can be adapted for missions that require heavier payloads or those that prioritize longer endurance.

UAVs are typically driven by electric motors and propelled by electrical energy stored in a battery. As their size increases, there are also UAVs that are propelled by fossil fuels in combination with combustion engines or jet engines. However, only electric-propelled UAVs are considered in this study. Numerous modeling approaches have been proposed to describe the energy consumption of electric-propelled UAVs, ranging from high-level empirical models to detailed physics-based models.Zhang et al. [45] and Muli et al. [28] review energy consumption models (ECMs) of electric-propelled UAVs and classify them into integrated models, regression models, and component models. *Integrated models* combine various aerodynamic and design aspects into a single critical parameter, the lift-to-drag ratio, to represent energy efficiency. For instance, D'Andrea [8] integrated model introduces this approach by considering the mass, the velocity, the lift-drag-ratio, the power train efficiency, and the power consumption of the avionics, providing a broad yet cohesive estimation of energy usage for UAVs across different flight phases. This method is efficient for high-level planning, though it highly depend on the choice of the lift-to-drag ratio and neglects detailed forces, which limits the model to a specific operation case. *Component models* decompose energy consumption into separate segments, such as hovering, takeoff, landing, and cruising, to estimate energy more granularly. This approach allows detailed representations of energy requirements by considering individual forces, such as the aircraft's weight force and various drag forces. Stolaroff et al. [37] apply a two-component model that includes the thrust required to compensate for weight and to counteract parasite drag. While this model can reflect variations in power demands across different phases of a flight, it may be complex to parameterize accurately and often require substantial empirical data for calibration. *Regression models* rely on empirical data from field tests, such as the work of Alyassi et al. [3], who utilize nonlinear regression with multiple variables, including payload mass, velocity, acceleration and wind conditions, to predict energy consumption. These models are useful in capturing energy requirements in real-world settings, especially where environmental factors significantly impact performance. By fitting data to real-world conditions, regression models can produce realistic estimations for specific UAVs and operational parameters. However, they are limited by the data available and may not generalize well to different UAV designs or operation scenarios [28, 45].

Asti et al. [4] propose a different approach to develop an energy-efficient obstacle avoidance. Here the change of kinetic and potential energy is used to evaluate the efficiency of a maneuver. This approach is simple and does not need further insight into the UAV design besides the total mass of the UAV. While it can evaluate the efficiency of a maneuver, it is not suitable for accurately estimating energy consumption.

In contrast to the mentioned models, we adopt a modular component-based approach, where the energy consumption is modeled by considering key components of the power train such as the lithium-ion battery (LIB), electric speed controllers (ESCs), brushless direct current (BLDC) motors and rotors. This level of abstraction allows for greater accuracy and flexibility, allowing the model to be adapted for different UAV configurations and use cases. Combined with an accurate model of the UAV dynamics, this model can be adapted to meet our requirements for accuracy, generalizability, and computational efficiency. By modeling the individual components, not only specific maneuvers are considered, but rather a variety of maneuvers. This allows for dynamic operations without having to discretize into different flight phases. Meanwhile, we aim to use common data sheet information, while only relying on few test flights to identify or calibrate model parameters.

This study is structured as follows: Section II details the modeling of multicopter UAVs, covering the vehicle's dynamics and physical properties. Section III presents the modeling of the energy consumption of electric-propelled UAVs. Section IV introduces the sensor models, specifically the camera and LiDAR, and their impact on the UAV's performance. In Section V, these models are combined to be used in advanced mission planning and control applications. Section VI discusses the validation of the energy consumption model and examines the uncertainties introduced by environmental factors. Finally, Section VII provides conclusions and suggests future work based on the outcomes of this study.

II. Unmanned Aerial Vehicle Modeling

In the following, we look at rotary-wing UAVs (multicopters), which use motors with attached rotors to generate a downward thrust to take off or remain in flight. Their high maneuverability (capable to hover and fly at high or low speeds) makes them ideal for surveillance or monitoring missions. Multicopters have a multiplicity of arms, each equipped with a motor driving a fixed rotor. The rotors rotate either clockwise or counterclockwise in an alternating pattern to balance the system with regard to the drag moment generated by the rotors in stationary flight. The following mathematical formulations of the multicopter's *kinematics* and *dynamics* are based on [10, 22, 29, 32, 42]. To derive the multicopter model we assume:

Assumption 1. *The multicopter is axis-symmetric with respect to the body-fixed frame and it's body is nearly spherical.*

Assumption 2. *The multicopter's actuators, like the BLDC motors, ESCs and rotors are identical.*

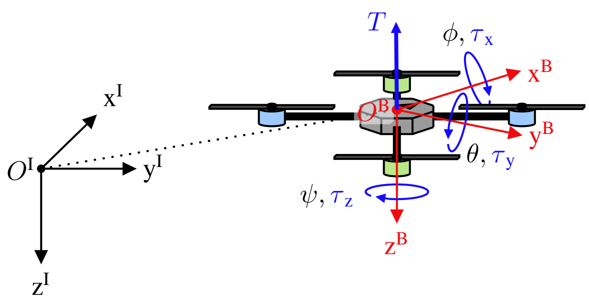

Fig. 1. Frames of reference (black: inertial frame, red: body-fixed frame); Forces and torques acting on the body's center of mass (blue)

A. Multicopter Kinematics

We define two frames of reference, shown in Fig. 1. The inertial frame of reference is an earth-fixed north-east-down frame and its origin O^{I} is attached to the earth's surface. The body-fixed frame is a forward-right-down frame and its origin O^{B} is attached to the multicopter's center of mass. Both frames of reference are right-handed coordinate systems.

The multicopter is a six-degree-of-freedom (6 DOF) underactuated system, meaning that the rotational system is fully actuated, meanwhile, the translational system is underactuated. The position $\mathbf{P}^{\mathrm{I}} = (x, y, z)^\top$ of the multicopter represents the distance between the origins of the reference frames and is defined in the inertial frame. The orientation $\mathbf{\Psi} = (\phi, \theta, \psi)^\top$ of the multicopter is represented by Euler angles, also known as yaw angle ψ (rotation around the z-axis), pitch angle θ (rotation around the y-axis), and roll angle ϕ (rotation around the x-axis). It is defined as the rotation between the inertial and body-fixed frame. Since some values are measured in the inertial frame and others in the body-fixed frame, we define two transformation matrices to convert values from the body-fixed frame to the inertial frame. A vector, defined in the inertial frame, is obtained by the product of the corresponding vector in the body-fixed frame and the rotation matrix

$$\mathbf{R}_{\mathrm{B}}^{\mathrm{I}} = \begin{bmatrix} \mathrm{c}(\psi)\mathrm{c}(\theta) & \mathrm{c}(\psi)\mathrm{s}(\theta)\mathrm{s}(\phi) - \mathrm{s}(\psi)\mathrm{c}(\phi) & \mathrm{c}(\psi)\mathrm{s}(\theta)\mathrm{c}(\phi) + \mathrm{s}(\psi)\mathrm{s}(\phi) \\ \mathrm{s}(\psi)\mathrm{c}(\theta) & \mathrm{s}(\psi)\mathrm{s}(\theta)\mathrm{s}(\phi) + \mathrm{c}(\psi)\mathrm{c}(\phi) & \mathrm{s}(\psi)\mathrm{s}(\theta)\mathrm{c}(\phi) - \mathrm{c}(\psi)\mathrm{s}(\phi) \\ -\mathrm{s}(\theta) & \mathrm{c}(\theta)\mathrm{s}(\phi) & \mathrm{c}(\theta)\mathrm{c}(\phi) \end{bmatrix},$$

where $\mathrm{s}, \mathrm{c}, \mathrm{t}$ are abbreviations for $\sin, \cos, \tan$. Accordingly, the translational velocity $\dot{\mathbf{P}}^{\mathrm{I}} = (v_{\mathrm{x}}, v_{\mathrm{y}}, v_{\mathrm{z}})^\top$ is obtained by

$$\dot{\mathbf{P}}^{\mathrm{I}} = \mathbf{R}_{\mathrm{B}}^{\mathrm{I}} \dot{\mathbf{P}}^{\mathrm{B}},$$

where $\dot{\mathbf{P}}^{\mathrm{B}}$ is the velocity vector in the body-fixed frame. Likewise, the euler rates $\dot{\mathbf{\Psi}} = (\dot{\phi}, \dot{\theta}, \dot{\psi})^\top$ are obtained by

$$\dot{\mathbf{\Psi}} = \mathbf{R}_{\Psi}\, \boldsymbol{\omega}^{\mathrm{B}}. \tag{1}$$

Here, the angular velocity $\omega^{\mathrm{B}} = (\omega_{\mathrm{x}}, \omega_{\mathrm{y}}, \omega_{\mathrm{z}})^\top$ in the body-fixed frame is transformed by the angular transformation matrix

$$\mathbf{R}_{\Psi} = \begin{bmatrix} 1 & \mathrm{s}(\phi)\mathrm{t}(\theta) & \mathrm{c}(\phi)\mathrm{t}(\theta) \\ 0 & \mathrm{c}(\phi) & -\mathrm{s}(\phi) \\ 0 & \mathrm{s}(\phi)/\mathrm{c}(\theta) & \mathrm{c}(\phi)/\mathrm{c}(\theta) \end{bmatrix}.$$

Remark 1. *We constrain the Euler angles $\phi, \theta \in \left(-\frac{\pi}{2}, \frac{\pi}{2}\right)$ to avoid singularities in $\mathbf{R}_{\Psi}$. This assumption is feasible if the multicopter does not perform aggressive maneuvers [12, 32].*

B. Multicopter Dynamics

The motion of the multicopter is divided into a rotational and a translational motion component. To control the rotational motion, we apply torque to the multicopter's center of mass. Fig. 1 shows the controllable torques $\boldsymbol{\tau}^{\mathrm{B}} = (\tau_{\mathrm{x}}, \tau_{\mathrm{y}}, \tau_{\mathrm{z}})^\top$, as well as the combined thrust T of all rotors, which is used to control the translational motion.

The rotational equations of motion in the body-fixed frame derive from the Newton-Euler formalism

$$\boldsymbol{\tau}^{\mathrm{B}} = \mathbf{J}\dot{\boldsymbol{\omega}}^{\mathrm{B}} + \boldsymbol{\omega}^{\mathrm{B}} \times \mathbf{J}\,\boldsymbol{\omega}^{\mathrm{B}} + \boldsymbol{\tau}_{\mathrm{G}}^{\mathrm{B}} + \boldsymbol{\tau}_{\mathrm{D}}^{\mathrm{B}}, \tag{2}$$

where $\dot{\boldsymbol{\omega}}^{\mathrm{B}} = (\dot{\omega}_{\mathrm{x}}, \dot{\omega}_{\mathrm{y}}, \dot{\omega}_{\mathrm{z}})^\top$ is the angular acceleration. Due to Assumption 1, the inertia tensor $\mathbf{J} = \mathrm{diag}\{J_{\mathrm{xx}}, J_{\mathrm{yy}}, J_{\mathrm{zz}}\}$ has only entries on the diagonal representing the moments of inertia around the body axes. The gyroscopic effect of the angular motion of the rotors is considered by

$$\boldsymbol{\tau}_{\mathrm{G}}^{\mathrm{B}} = \boldsymbol{\omega}^{\mathrm{B}} \times \begin{pmatrix} 0 \\ 0 \\ J_{\mathrm{r}}\,\Omega_{\mathrm{r}} \end{pmatrix},$$

where J_{r} and Ω_{r} are the inertia moment of a rotor and the difference in rotor speeds, respectively. The drag torque

$$\boldsymbol{\tau}_{\mathrm{D}}^{\mathrm{B}} = \mathbf{D}_{\tau}\boldsymbol{\omega}^{\mathrm{B}}$$

accounts for the air drag, which is approximately proportional to the angular velocity ω^{B} and depends on the angular air resistance coefficients within matrix $\mathbf{D}_{\tau} = \mathrm{diag}\{c_{\tau\mathrm{x}}, c_{\tau\mathrm{y}}, c_{\tau z}\}$.

The translational equations of motion in the inertial frame derive from Newton's second law

$$m\,\ddot{\mathbf{P}}^{\mathrm{I}} = \mathbf{F}_{\mathrm{G}}^{\mathrm{I}} + \mathbf{R}_{\mathrm{B}}^{\mathrm{I}}\,\mathbf{F}^{\mathrm{B}} - \mathbf{F}_{\mathrm{D}}^{\mathrm{I}}, \tag{3}$$

where $\ddot{\mathbf{P}}^{\mathrm{I}} = (\ddot{x}, \ddot{y}, \ddot{z})^\top$ is the translational acceleration. The gravitational force

$$\mathbf{F}_{\mathrm{G}}^{\mathrm{I}} = (0, 0, m\,\mathrm{g})^\top,$$

depends on the total mass of the body m as well as the acceleration of free fall g, while the non-gravitational force

$$\mathbf{F}^{\mathrm{B}} = (0, 0, -T)^\top,$$

results from the thrust T of all rotors. Lastly, the drag force

$$\mathbf{F}_{\mathrm{D}}^{\mathrm{I}} = \mathbf{D}_{\mathrm{F}}\mathbf{v}_{\mathrm{a}}^{\mathrm{I}}$$

accounts for the air drag, which is approximately proportional to the air velocity $\mathbf{v}_\mathrm{a}^\mathrm{I}$ and further depends on the resistance coefficients within the matrix $\mathbf{D}_\mathrm{F} = \mathrm{diag}\{c_\mathrm{Fx}, c_\mathrm{Fy}, c_\mathrm{Fz}\}$ [15]. Here, the air velocity $\mathbf{v}_\mathrm{a}^\mathrm{I} = \dot{\mathbf{P}}^\mathrm{I} - \mathbf{v}_\mathrm{w}^\mathrm{I}$ relates the UAV's translational velocity $\dot{\mathbf{P}}^\mathrm{I}$ to the wind velocity $\mathbf{v}_\mathrm{w}^\mathrm{I} = (v_\mathrm{w,x}, v_\mathrm{w,y}, v_\mathrm{w,z})^\top$.

C. Multicopter Models

We rearrange and combine (1), (2) and (3) to obtain the general nonlinear state space multicopter model

$$\dot{\mathbf{x}}_\mathrm{u} = \mathbf{f}_\mathrm{u}(\mathbf{x}_\mathrm{u}, \mathbf{u}_\mathrm{u}, \mathbf{d}_\mathrm{u}) + \mathbf{\Gamma}_\mathrm{u,x}, \tag{4}$$

with the state $\mathbf{x}_\mathrm{u} = (x, y, z, v_\mathrm{x}, v_\mathrm{y}, v_\mathrm{z}, \phi, \theta, \psi, \omega_\mathrm{x}, \omega_\mathrm{y}, \omega_\mathrm{z})^\top$, the input $\mathbf{u}_\mathrm{u} = (T, \tau_\mathrm{x}, \tau_\mathrm{y}, \tau_\mathrm{z}, \Omega_\mathrm{r})^\top$ and the external disturbance $\mathbf{d}_\mathrm{u} = (v_\mathrm{w,x}, v_\mathrm{w,y}, v_\mathrm{w,z})^\top$. Here, the right-hand side reads

$$\mathbf{f}_\mathrm{u}(\mathbf{x}_\mathrm{u}, \mathbf{u}_\mathrm{u}, \mathbf{d}_\mathrm{u}) = \begin{pmatrix} \dot{\mathbf{P}}^\mathrm{I} \\ \frac{1}{m}\left(\mathbf{F}_\mathrm{G}^\mathrm{I} + \mathbf{R}_\mathrm{B}^\mathrm{I}\,\mathbf{F}^\mathrm{B} - \mathbf{F}_\mathrm{D}^\mathrm{I}\right) \\ \mathbf{R}_\Psi\,\boldsymbol{\omega}^\mathrm{B} \\ \mathbf{J}^{-1}\left(\boldsymbol{\tau}^\mathrm{B} - \boldsymbol{\omega}^\mathrm{B} \times \mathbf{J}\,\boldsymbol{\omega}^\mathrm{B} - \boldsymbol{\tau}_\mathrm{G}^\mathrm{B} - \boldsymbol{\tau}_\mathrm{D}^\mathrm{B}\right) \end{pmatrix}.$$

Additionally, $\mathbf{\Gamma}_\mathrm{u,x}$ represents unknown uncertainties, resulting from modeling inaccuracies and turbulences.

As the path planner in [14], many real-time applications require discrete-time linear models. Therefore, we derive in Appendix A, the corresponding multicopter model

$$\mathbf{x}_\mathrm{u}(k+1) = \mathbf{A}_\mathrm{d,u}\,\mathbf{x}_\mathrm{u}(k) + \mathbf{B}_\mathrm{d,u}\,\tilde{\mathbf{u}}_\mathrm{u}(k) + \mathbf{H}_\mathrm{d,u}\,\mathbf{d}_\mathrm{u}(k) + \mathbf{\Gamma}_\mathrm{u,x}(k), \tag{5}$$

where $\mathbf{A}_\mathrm{d,u}$, $\mathbf{B}_\mathrm{d,u}$ and $\mathbf{H}_\mathrm{d,u}$ are the discrete-time system, input and disturbance matrices. For the chosen set point, the hovering state $\mathbf{x}_\mathrm{u,SP} = (0, \ldots, 0)^\top$ without any external disturbance $\mathbf{d}_\mathrm{u,SP} = (0, \ldots, 0)^\top$, the multicopter maintains its position and the thrust $T_\mathrm{SP} = m\,g$ compensates for the weight force. Meanwhile, the input is reduced to

$$\tilde{\mathbf{u}}_\mathrm{u} = (L, \tau_x, \tau_y, \tau_z)^\top,$$

where the lift L is the thrust component acting in negative z^I-direction, which is added to the hovering thrust T_SP.

D. Adapting For Specific Multicopter Configurations

The various multicopter configurations differ in their positioning and number of rotors. Each rotor is fixed to a motor, rotating with the motor speed $\Omega_i,\ i \in \{1, \ldots, N_\mathrm{M}\}$, where N_M is the number of motors. To adapt the generalized multicopter model for a specific multicopter configuration, the input has to be defined depending on these motor speeds. In the following, we define clockwise rotations as positive and counterclockwise rotations as negative. Accordingly, the difference in rotor speeds is given by

$$\Omega_\mathrm{r} = \sum_{i=1}^{N_\mathrm{M}} \mathrm{sign}(\Omega_i)\,\Omega_i. \tag{6}$$

Each rotor generates an upwards-pointing aerodynamic force

$$F_i = k_\mathrm{F}\,\Omega_i^2, \quad \forall\, i \in \{1, \ldots, N_\mathrm{M}\}, \tag{7}$$

and a rotation-counteracting aerodynamic drag torque

$$M_i = k_\mathrm{M}\,\Omega_i^2, \quad \forall\, i \in \{1, \ldots, N_\mathrm{M}\}, \tag{8}$$

where k_F and k_M are the aerodynamic force and torque constants and Assumption 3 applies [10, 22, 29].

Assumption 3. *For simplicity, we assume that the aerodynamic parameters k_F and k_M are constant. However, in reality, they depend on the rotor speed, airflow, and air pressure.*

According to Fig. 2, the thrust

$$T = \sum_{i=1}^{N_\mathrm{M}} F_i, \tag{9}$$

combines the N_M forces, defined by (7). Meanwhile, the torques are given by

$$\tau_\mathrm{x} = \sum_{i=1}^{N_\mathrm{M}} -l_{\mathrm{y},i}\,F_i, \quad \tau_\mathrm{y} = \sum_{i=1}^{N_\mathrm{M}} l_{\mathrm{x},i}\,F_i, \quad \tau_\mathrm{z} = \sum_{i=1}^{N_\mathrm{M}} -\mathrm{sign}(\Omega_i)\,M_i, \tag{10}$$

where $\mathbf{l}_i^\mathrm{B} = (l_{\mathrm{x},i}, l_{\mathrm{y},i})^\top$ indicates the i^th rotor's position.

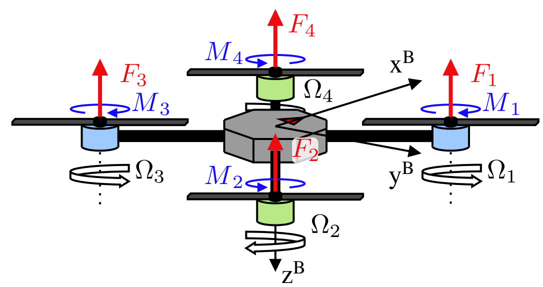

Fig. 2. Aerodynamic forces and torques of a quadcopter in X-configuration

E. Vehicle Capabilities

In order to consider the vehicle's limits, the model is constrained. It is common practice to divide the velocity of a multicopter into two parts: the ground velocity

$$v_\mathrm{g} = \sqrt{v_\mathrm{x}^2 + v_\mathrm{y}^2}, \quad \text{s.t. } v_\mathrm{g} \le v_\mathrm{g,max}$$

and the climb/descent velocity

$$v_\mathrm{c} = |v_\mathrm{z}|, \quad \text{s.t. } v_\mathrm{c} \le v_\mathrm{c,max},$$

which are constrained by their respective maximum values $v_\mathrm{g,max}$ and $v_\mathrm{c,max}$. Moreover, the tilt angle

$$\alpha = \cos^{-1}(\cos(\phi)\cos(\theta)) \approx \sqrt{\phi^2 + \theta^2},$$
$$\text{s.t. } \alpha \le \alpha_\mathrm{max},$$

is constrained by its maximum value α_max and Remark 1 must be considered to avoid singularities. Constraints on the angular rates ω^B should be included if the multicopter is equipped with sensible instruments.

To represent the motors' capabilities, the input is constrained using (9), (10) and the motor speed limits

$$0 \le \Omega_i \le \Omega_\mathrm{max}, \quad \forall\, i \in \{1, \ldots, N_\mathrm{M}\}.$$

Remark 2. *The approximation error of the linearized model decreases if the yaw angle ψ is constrained to $\psi \approx 0$.*

III. Energy Consumption Modeling

In this study, we employ a component modeling approach for the energy consumption modeling as the detailed model design enables us to consider different UAV designs, environmental influences, and use cases. In combination with an accurate UAV model, a component model is adapted to fulfill our requirements of accuracy, generalizability, and simulation resource demand. In the following, we derive the individual components of the power train and combine them to obtain the ECM for electric-propelled UAVs.

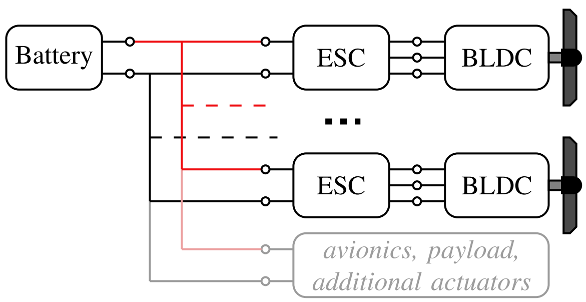

Fig. 3. Common power train of an electric-propelled UAV

Fig. 3 shows the power train of an electric-propelled UAV, which is divided into three prominent components. The lithium-ion battery (LIB) stores the energy, which the electric speed controller (ESC) transfers to the brushless direct current (BLDC) motor, which drives a fixed rotor. The ESC controls the BLDC motor, depending on a pulse width modulation (PWM) control command provided by the flight controller. The component model could be extended by including the avionics, the payload, or additional actuators. However, the complexity increase is only meaningful if they consume significant energy compared to the BLDC motors.

A. Lithium-Ion Battery

The first component is the LIB, whose state is described by the state of charge SoC and the battery voltage u_b. Hussein and Batarseh [17] and Zhou et al. [46] review several modeling approaches for LIB cells. We adopt an equivalent circuit model due to its descriptive formulation, possible short simulation run-time, and good estimation accuracy. Commonly, LIBs consist of multiple cells, which can be connected in series and parallel, as shown in Fig. 4. For simplification, we assume:

Assumption 4. *All LIB cells are identical and the load is distributed evenly.*

Considering Assumption 4, the number of cells connected in series N_S and parallel N_P define the battery voltage u_b and battery current i_b by

$$u_\mathrm{b} = N_\mathrm{S}\, u_\mathrm{c}, \qquad i_\mathrm{b} = N_\mathrm{P}\, i_\mathrm{c}, \tag{11}$$

where u_c and i_c are the LIB cells' voltage and current.

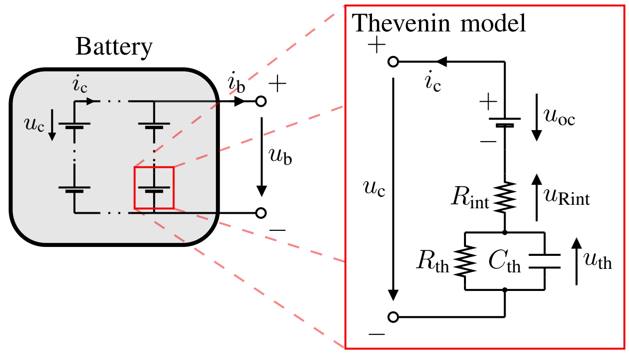

Fig. 4. Simplified battery circuit & Thevenin model

We define the portion of the already discharged battery charge, also called the depth of discharge, as

$$\mathrm{DoD} = \mathrm{DoD}_0 + \frac{\eta_\mathrm{b}}{Q_\mathrm{b}} \int i_\mathrm{b}\,\mathrm{d}t, \tag{12}$$

where DoD_0 is the initial depth of discharge and $\eta_\mathrm{b}, Q_\mathrm{b}, i_\mathrm{b}$ are the battery's efficiency, capacity and current. This method is called Coulomb counting and is characterized by its simplicity and performance [30]. Commonly, this method is used to describe the state of charge

$$\mathrm{SoC} = 1 - \mathrm{DoD}, \tag{13}$$

which is the portion of the remaining battery charge.

For the LIB cell model, we apply a first-order equivalent circuit model, also known as Thevenin model. It describes the LIB cell behavior accurately, while the simulation run-time, the complexity, and the needed information about the inner processes of the LIB cell are limited. Fig. 4 illustrates the Thevenin model consisting of an ohmic resistance R_int, an ideal voltage source u_oc, and an RC parallel network $R_\mathrm{th} \| C_\mathrm{th}$ connected in series. The total internal resistance is divided into the ohmic resistance R_int and the polarization resistance R_th. If no load is applied, the LIB cell voltage u_c equals the open circuit voltage u_oc. The polarization RC network describes effects resulting from chemical reactions in the electrode surfaces and the ion mass transfer inside the LIB cell [16, 30]. According to Kirchhoff's circuit laws, we define the characteristic equations of the Thevenin model

$$\begin{aligned}
\frac{\mathrm{d}}{\mathrm{d}t} u_\mathrm{th} &= -\frac{1}{R_\mathrm{th}\, C_\mathrm{th}}\, u_\mathrm{th} + \frac{1}{C_\mathrm{th}}\, i_\mathrm{c}, \\
u_\mathrm{c} &= u_\mathrm{oc} - u_\mathrm{th} - R_\mathrm{int}\, i_\mathrm{c},
\end{aligned}$$

where we insert (11), while considering (12) to obtain the LIB's characteristic equations

$$\begin{aligned}
\frac{\mathrm{d}}{\mathrm{d}t} \mathrm{DoD} &= \frac{\eta_\mathrm{b}}{Q_\mathrm{b}}\, i_\mathrm{b}, \\
\frac{\mathrm{d}}{\mathrm{d}t} u_\mathrm{th} &= -\frac{1}{R_\mathrm{th}\, C_\mathrm{th}}\, u_\mathrm{th} + \frac{1}{N_\mathrm{P}\, C_\mathrm{th}}\, i_\mathrm{b}, \\
u_\mathrm{b} &= N_\mathrm{S} \left(u_\mathrm{oc} - u_\mathrm{th} - \frac{R_\mathrm{int}}{N_\mathrm{P}}\, i_\mathrm{b} \right).
\end{aligned} \tag{14}$$

Remark 3. *Since the polarization effects are only considered by one RC-network, the LIB cell behavior at the end of discharge phase can not be reproduced accurately.*

To increase the accuracy of the LIB cell model, we define the ideal voltage source u_{oc} as dependent on the depth of discharge DoD. Fig. 5 shows a generalized discharge curve of a LIB cell (black graph) and the cutoff depth of discharge $\overline{\mathrm{DoD}}_{\mathrm{cutoff}}$ (red dot), set to 85%, which limits the depth of discharge to avoid over-discharging.

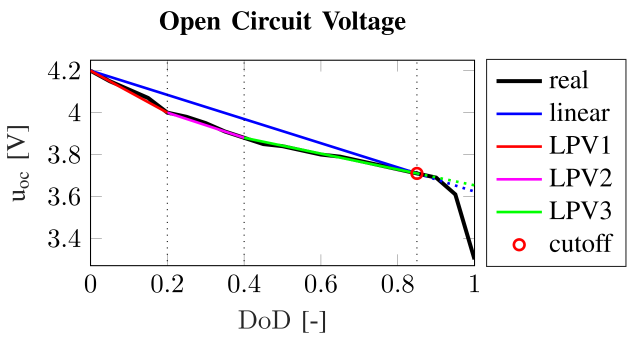

Fig. 5. Generalized discharge curve of a LiPo cell (black) [11], linear approximation (blue), and LPV approximations (red, magenta, green)

Remark 4. *The actual discharge curve of a LIB cell is highly individual and can differ from the black graph in Fig. 5 due to external circumstances (temperature, state of health, discharge rate) and technological differences, et cetera.*

According to the blue graph, the linear approximation

$$u_{\mathrm{oc}} = b_0 + b_1\,\mathrm{DoD} \quad \text{for} \quad 0 \le \mathrm{DoD} \le \overline{\mathrm{DoD}}_{\mathrm{cutoff}}. \tag{15}$$

is parameterized by the open circuit voltage parameters b_0 and b_1. Due to the non-linearity of the discharge curve, we propose to define a piece-wise linear function

$$u_{\mathrm{oc}} = \begin{cases} b_{0,1} + b_{1,1}\,\mathrm{DoD} \text{ for } \overline{\mathrm{DoD}}_0 \le \mathrm{DoD} \le \overline{\mathrm{DoD}}_1, \\ b_{0,2} + b_{1,2}\,\mathrm{DoD} \text{ for } \overline{\mathrm{DoD}}_1 \le \mathrm{DoD} \le \overline{\mathrm{DoD}}_2, \\ b_{0,3} + b_{1,3}\,\mathrm{DoD} \text{ for } \overline{\mathrm{DoD}}_2 \le \mathrm{DoD} \le \overline{\mathrm{DoD}}_3, \end{cases} \tag{16}$$

where the index $i \in \{1, \ldots, 3\}$ indicates the active LPV battery model. Depending on this index the corresponding parameters $b_{0,i}$, $b_{1,i}$ and the thresholds $\left[\overline{\mathrm{DoD}}_{i-1}, \overline{\mathrm{DoD}}_i\right]$ are chosen to fit the red-, magenta-, and green-colored graphs in Fig. 5, respectively.

B. Electric Speed Controller

The second component is the ESC, which connects the LIB with the BLDC motor and controls the BLDC motor, depending on the PWM control command s_{PWM}. Since the BLDC motor will be modeled as a simplified direct current (DC) motor, we model the ESC as a DC-to-DC converter, which regulates the voltage supply to a DC motor. Then, the ESC converts the battery voltage u_{b} to the DC motor's voltage

$$u_{\mathrm{DC}} = f_{\mathrm{ESC}}(s_{\mathrm{PWM}})\,u_{\mathrm{b}},$$

depending on the function $f_{\mathrm{ESC}}(s_{\mathrm{PWM}})$, which is approximately a linear function [25]. In order to formulate the relation between the DC motor's supply power and the ESC's input current

$$i_{\mathrm{ESC}} = \frac{1}{\eta_{\mathrm{ESC}}} f_{\mathrm{ESC}}(s_{\mathrm{PWM}})\,i_{\mathrm{DC}} = \frac{p_{\mathrm{DC}}}{\eta_{\mathrm{ESC}}\,u_{\mathrm{b}}}, \tag{17}$$

we consider the ESC's efficiency η_{ESC} and follow the energy conservation law

$$p_{\mathrm{ESC}}\,\eta_{\mathrm{ESC}} = p_{\mathrm{DC}},$$

where $p_{\mathrm{ESC}} = i_{\mathrm{ESC}}\,u_{\mathrm{b}}$ is the power supplied to the ESC.

C. Brushless Direct Current Motor with a fixed Rotor

The third component is the BLDC motor. It is a special kind of synchronous machine, which is controlled by an ESC. According to a commutation logic, which depends on the rotor position, direct currents are applied to the three input wires of the BLDC motor. By this, the magnetic poles of the stator coils align with the rotor monopoles to initiate or maintain the rotation of the rotor. For more information, see [5].

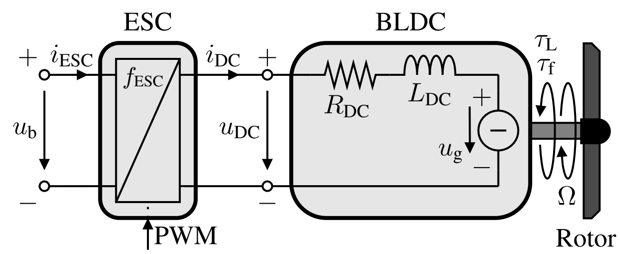

Fig. 6. Simplified ESC-BLDC circuit

Fig. 6 shows a simplified ESC-BLDC circuit. Since the structure and dynamics of a BLDC motor are complex and not continuous, we approximate its power consumption by a simplified DC motor with a fixed rotor, based on [12, 21, 27]. Here, we assume:

Assumption 5. *The BLDC motor is driving at a constant speed and the motor friction torque is negligible due to liquid lubrication.*

As shown in Fig. 6, the simplified DC motor is built from elementary electrical components. The resistances of the motor and the inductance of the coils are summarized as the motor's internal resistance R_{DC} and the motor's inductance L_{DC}. An ideal power sink $u_{\mathrm{g}} = \Omega / K_{\mathrm{V}}$ represents the transformation of electrical power to mechanical power, where K_{V} is the voltage constant of the motor and Ω is the motor speed. According to Kirchhoff's circuit laws, the motor voltage u_{DC} is given by

$$\begin{aligned} u_{\mathrm{DC}} = u_{\mathrm{R}} + u_{\mathrm{L}} + u_{\mathrm{g}} &= R_{\mathrm{DC}}\,i_{\mathrm{DC}} + L_{\mathrm{DC}} \frac{\mathrm{d}\,i_{\mathrm{DC}}}{\mathrm{d}\,t} + \frac{1}{K_{\mathrm{V}}}\Omega \\ &= R_{\mathrm{DC}}\,i_{\mathrm{DC}} + \frac{1}{K_{\mathrm{V}}}\Omega, \end{aligned} \tag{18}$$

where the motor current reads

$$\begin{aligned} i_{\mathrm{DC}} = \frac{1}{K_\tau}\tau_M &= \frac{1}{K_\tau}\left(J_{\mathrm{r}} \frac{\mathrm{d}\,\Omega(t)}{\mathrm{d}t} + D_{\mathrm{f}}\,\Omega + \tau_{\mathrm{f}} + \tau_{\mathrm{L}}\right) \\ &= K_{\mathrm{V}}\,\left(D_{\mathrm{f}}\,\Omega + \tau_{\mathrm{L}}\right). \end{aligned} \tag{19}$$

It depends on the motor torque τ_{M} and the motor's torque constant K_τ, which is approximated by $K_\tau = 1/K_{\mathrm{V}}$. The motor torque τ_{M} represents the torque required to change the motor speed $J_{\mathrm{r}} \frac{\mathrm{d}\,\Omega}{\mathrm{d}t}$ and to compensate for the viscous damping of the motor $D_{\mathrm{f}}\,\Omega$, the motor friction torque τ_{f} and the load friction torque τ_{L}. Here, J_{r} is the moment of inertia of the rotor and D_f is the viscous damping factor of the motor. According to (8), the load friction torque $\tau_\mathrm{L} = k_\mathrm{M}\,\Omega^2$ equals the aerodynamic torque produced by the rotor. Equations (18) and (19) are simplified according to Assumption 5 to obtain the power consumption of the BLDC motor

$$\begin{aligned} p_\mathrm{DC} &= u_\mathrm{DC}\, i_\mathrm{DC} \\ &= \underbrace{R_\mathrm{DC}\, K_\mathrm{V}^2\, \left(D_\mathrm{f}\,\Omega + k_\mathrm{M}\,\Omega^2\right)^2}_{P_\mathrm{el}} + \underbrace{D_\mathrm{f}\,\Omega^2}_{P_\mathrm{mech}} + \underbrace{k_\mathrm{M}\,\Omega^3}_{P_\mathrm{out}}. \end{aligned} \quad (20)$$

It consists of the electrical power loss P_el, the mechanical power loss P_mech and the mechanical output power P_out.

D. Combined Energy Consumption Model

We combine all three components of the power train to derive the ECM for electric-propelled UAVs. Fig. 3 illustrates the standard circuit, where the ESC-BLDC connections are connected in parallel to the battery. To derive the ECM, we define the motor speeds and external power consumption $\mathbf{u}_\mathrm{e} = (\Omega_1, \ldots, \Omega_{N_\mathrm{M}})^\top$ as input and the state contains the depth of discharge DoD, and the polarization voltage u_th. Further, the output contains the state of charge SoC, the battery voltage u_b and the battery current i_b.

Considering (14), (17) and (20), the battery current

$$i_\mathrm{b} = \sum_{i=1}^{N_\mathrm{M}} i_{\mathrm{ESC},i} = \frac{1}{u_\mathrm{b}(\mathrm{DoD}, u_\mathrm{th}, i_\mathrm{b})} \sum_{i=1}^{N_\mathrm{M}} \frac{p_{\mathrm{DC},i}(\Omega_i)}{\eta_{\mathrm{ESC},i}},$$

is defined as the sum of the input currents of the ESCs $i_{\mathrm{ESC},i}$, where N_M defines the number of BLDC motors. If the BLDC motors do not consume any power, the battery current equals zero. Therefore, we get

$$i_\mathrm{b} = \tilde{i} - \sqrt{\tilde{i}^2 - \frac{N_\mathrm{P}}{N_\mathrm{S}\, R_\mathrm{int}} \sum_{i=1}^{N_\mathrm{M}} \frac{p_{\mathrm{DC},i}(\Omega_i)}{\eta_{\mathrm{ESC},i}}}, \quad (21)$$

where $\tilde{i}$ substitutes for $\tilde{i} = \frac{N_\mathrm{P}\,(u_\mathrm{oc}(\mathrm{DoD}) - u_\mathrm{th})}{2\, R_\mathrm{int}}$.

Remark 5. *The power consumption of other components, like the avionics, the payload, or additional actuators can be added in (21) to the sum of power terms if they consume a significant amount of power, compared to the BLDC motors.*

With (12), (13), (14) and (21), we obtain the nonlinear state space ECM for electric propelled UAVs by

$$\begin{aligned} \dot{\mathbf{x}}_\mathrm{e} &= \mathbf{f}_\mathrm{e}(\mathbf{x}_\mathrm{e}, \mathbf{u}_\mathrm{e}) + \mathbf{\Gamma}_\mathrm{e,x}, \\ \mathbf{y}_\mathrm{e} &= \mathbf{g}_\mathrm{e}(\mathbf{x}_\mathrm{e}, \mathbf{u}_\mathrm{e}) + \mathbf{\Gamma}_\mathrm{e,y}, \end{aligned} \quad (22)$$

with the state $\mathbf{x}_\mathrm{e} = (\mathrm{DoD}, u_\mathrm{th})^\top$, the input $\mathbf{u}_\mathrm{e} = (\Omega_1, \ldots, \Omega_{N_\mathrm{M}})^\top$ and the output $\mathbf{y}_\mathrm{e} = (\mathrm{SoC}, u_\mathrm{b}, i_\mathrm{b})^\top$, where the right-hand sides of (22) read

$$\mathbf{f}_\mathrm{e}(\mathbf{x}_\mathrm{e}, \mathbf{u}_\mathrm{e}) = \begin{pmatrix} \dfrac{\eta_\mathrm{b}}{Q_\mathrm{b}}\, i_\mathrm{b}(\cdot) \\ -\dfrac{1}{R_\mathrm{th}\, C_\mathrm{th}}\, u_\mathrm{th} + \dfrac{1}{N_\mathrm{P}\, C_\mathrm{th}}\, i_\mathrm{b}(\cdot) \end{pmatrix},$$

$$\mathbf{g}_\mathrm{e}(\mathbf{x}_\mathrm{e}, \mathbf{u}_\mathrm{e}) = \begin{pmatrix} 1 - \mathrm{DoD} \\ N_\mathrm{S}\left(u_\mathrm{oc}(\mathrm{DoD}) - u_\mathrm{th} - \dfrac{R_\mathrm{int}}{N_\mathrm{P}}\, i_\mathrm{b}(\cdot)\right) \\ i_\mathrm{b}(\cdot) \end{pmatrix}.$$

Here, $i_\mathrm{b}(\mathrm{DoD}, u_\mathrm{th}, \Omega_1, \ldots, \Omega_{N_\mathrm{M}})$ is defined by (21) and $u_\mathrm{oc}(\mathrm{DoD})$ can be ether selected according to (15) or (16) for the nonlinear or nonlinear parameter-varying (NPV) ECM. Further, $\mathbf{\Gamma}_\mathrm{e,x}$ and $\mathbf{\Gamma}_\mathrm{e,y}$ represent uncertainties, originating from modeling inaccuracies and external factors, as temperature changes.

Considering Assumption 2, the general ECM for electric-propelled UAVs is adjusted especially for multicopters to derive a fitting discrete-time LPV ECM in Appendix A. For the chosen set point, the hovering state with a fully charged battery $\mathbf{x}_\mathrm{e} = (0, \ldots, 0)^\top$, the thrust T_SP compensates for the weight force, resulting in equal motor seeds $\Omega_\mathrm{SP} = \sqrt{\frac{m\,g}{k_\mathrm{F}\, N_\mathrm{M}}}$ for all N_M motors. Due to (9) and the properties of linear models, the input $\mathbf{u}_\mathrm{e}$ is reduced to

$$\tilde{\mathbf{u}}_\mathrm{e} = \Delta T = T - T_\mathrm{SP},$$

which is the deviation of the thrust from the set point. After the linearization, discretization, and reduction, we obtain the discrete-time linear state-space multicopter ECM

$$\begin{aligned} \mathbf{x}_\mathrm{e}(k+1) &= \mathbf{A}_\mathrm{d,e}\, \mathbf{x}_\mathrm{e}(k) + \mathbf{B}_\mathrm{d,e}\, \tilde{\mathbf{u}}_\mathrm{e}(k) + \mathbf{E}_\mathrm{d,e} + \mathbf{\Gamma}_\mathrm{e,x}, \\ \mathbf{y}_\mathrm{e}(k) &= \mathbf{C}_\mathrm{d,e}\, \mathbf{x}_\mathrm{e}(k) + \mathbf{D}_\mathrm{d,e}\, \tilde{\mathbf{u}}_\mathrm{e}(k) + \mathbf{y}_\mathrm{e,SP} + \mathbf{\Gamma}_\mathrm{e,y}, \end{aligned}$$

where $\mathbf{A}_\mathrm{d,e}$, $\mathbf{B}_\mathrm{d,e}$, $\mathbf{C}_\mathrm{d,e}$ and $\mathbf{D}_\mathrm{d,e}$ are the discrete-time state-space matrices. Since the set point is not an equilibrium point, $\mathbf{E}_\mathrm{d,e} = \mathbf{f}_\mathrm{e}(\mathbf{x}_\mathrm{e,SP}, \mathbf{u}_\mathrm{c,SP})\,\Delta t$ and $\mathbf{y}_\mathrm{e,SP} = \mathbf{g}_\mathrm{e}(\mathbf{x}_\mathrm{e,SP}, \mathbf{u}_\mathrm{c,SP})$ are added as an offset for the energy consumption during hovering.

E. Power Train Capabilities

In order to prevent damage to the battery, the output of the ECM should be constrained by

$$\begin{aligned} \mathrm{SoC}_\mathrm{cutoff} \leq \mathrm{SoC} &\leq 1, \\ u_\mathrm{min}\, N_\mathrm{S} \leq\ u_\mathrm{b}\ &\leq u_\mathrm{max}\, N_\mathrm{S}, \\ -i_\mathrm{charge,max} \leq\ i_\mathrm{b}\ &\leq i_\mathrm{discharge,max}, \end{aligned}$$

where $\mathrm{SoC}_\mathrm{cutoff}$ is the cutoff state of charge, $(u_\mathrm{min}, u_\mathrm{max})$ are the voltage boundaries for a LIB cell and $(i_\mathrm{charge,max}, i_\mathrm{discharge,max})$ are the upper bound of the currents during charge and discharge.

IV. Sensor and Communication Models

Depending on the mission, UAVs are equipped with additional sensors, which often impose additional constraints on the distance to a given target to capture or the velocity of the UAV. For example, during surveillance missions it is necessary to maintain a maximum distance to the ground and a maximum ground velocity to ensure that the measurements are valid and complete. The most common sensor types are cameras and light detection and ranging sensors (LiDARs). Cameras are widely used for visual tasks such as aerial imaging and object detection, offering high resolution but are sensitive to lighting and weather conditions. LiDARs, in contrast, provide precise 3D mapping and perform well in low-visibility environments, though they are more data-intensive and costly. Each sensor imposes requirements on the UAV operations and the mission planning. Therefore, we derive the corresponding constraints for both sensor types in the following.

A. Camera Model

When using a camera for data collection, both the alignment with the target and the spatial resolution of the image R_I, must be considered. The spatial resolution for an image taken from a distance d

$$R_\mathrm{I} = I/L = \frac{I}{2\,d\,\tan\left(\gamma/2\right)},$$

which is expressed in pixels per meter, depends on the camera's image resolution I and field of view γ. To ensure a minimum spatial resolution $R_\mathrm{I,min}$, the UAV's distance d_t to its target must satisfy

$$d_\mathrm{t} = \|\mathbf{p}_\mathrm{t} - \mathbf{p}\|_2 \leq \frac{I}{2\,R_\mathrm{I,min}\,\tan\left(\gamma/2\right)}, \tag{23}$$

where $\mathbf{p}$ and $\mathbf{p}_\mathrm{t}$ are the positions of the UAV and its target.

Further, the alignment of the camera is defined by the angle

$$\chi = \arccos\left(\frac{\mathbf{p}_\mathrm{t} - \mathbf{p}}{\|\mathbf{p}_\mathrm{t} - \mathbf{p}\|_2}\,\mathbf{R}_\mathrm{B}^\mathrm{I}\,\mathbf{a}_\mathrm{c}^\mathrm{B}\right),$$

which measures how well the camera's view aligns with the target. Here, $\mathbf{a}_\mathrm{c}^\mathrm{B}$ is the normalized camera mounting vector in the body-fixed frame and the target gets centered in the image, when the alignment angle χ is minimized.

For a fixed camera setup (see Fig. 7a), capturing the target and the surrounding area of interest requires that the alignment angle remains below a threshold defined by

$$\chi \leq \gamma/2 - \arctan\left(\frac{L_\mathrm{t}}{2\,d_\mathrm{t}}\right),$$

where $L_\mathrm{t} \leq I/R_\mathrm{I,min}$ is the diameter of the area of interest.

In a simpler case, the camera is mounted on a controlled gimbal, adjusting $\mathbf{a}_\mathrm{c}^\mathrm{B}$ to track the target. In this case $\chi \approx 0$ and it is sufficient to maintain the UAV's flight altitude $z \leq z_\mathrm{t}$ above the target altitude z_t.

During surveillance missions, such as described by Di Franco and Buttazzo [9] and shown in Fig. 7b, the camera is often controlled to point towards the ground with the target distance $d_\mathrm{t} = |z_\mathrm{t} - z|$. Increasing the UAV's flight altitude, while considering (23), allows for a larger captured area. Depending on the image's aspect ratio ρ, the UAV's ground velocity v_g is constrained by

$$v_\mathrm{g} \leq \frac{2\,|z_\mathrm{t} - z|\,\tan\left(\gamma/2\right)\,\left(1-\delta_\mathrm{c}\right)}{\rho\,T_\mathrm{s,c}},$$

where $\delta_\mathrm{c} \in [0,1]$ is the overlap of successive images and $T_\mathrm{s,c}$ is camera's sampling period.

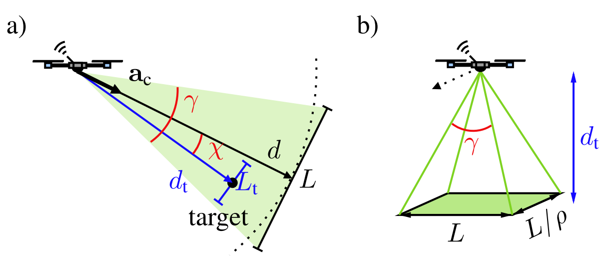

Fig. 7. a) Fixed camera; b) Controlled camera facing towards ground;

B. LIDAR Model

LiDARs measure distances by emitting laser pulses that reflect off objects and return to the receiver, allowing the system to calculate the distance based on the light's travel time. In combination with position and orientation data, the exact location of the point measurement is determined. By scanning across different directions, a precise 3D map of the environment, refastened by a point cloud, is created. The sensor's emitter and a receiver typically operate within a horizontal field of view γ_h and vertical field of view γ_v up to a defined effective LiDAR range r_L. Often both are mounted on a rotating axis to achieve a full scan of the horizontal plane $\gamma_\mathrm{h} = 2\,\pi$. The quality of these scans is expressed by the point cloud density R_l in points per square meters or by the spacing between points d_p. Those depend on the vertical and horizontal angular resolutions, V_res and H_res, as well as the distance to the target d_t [44]. In the following, we derive constraints on the UAV's operations for two different LiDAR use cases, shown in Fig. 8, ensuring valid data collection.

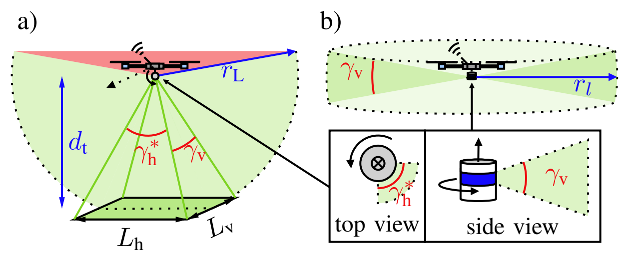

Fig. 8. a) LiDAR for vertical scanning; b) LiDAR for horizontal scanning;

For the first LiDAR configuration, the sensor is mounted on a gimbal to scan the vertical plane with its rotation axis parallel to the ground, as shown in Fig. 8a. This setup is typically used for ground measurements or mapping. To ensure adequate point cloud density $R_\mathrm{L} = N_\mathrm{p}/A_\mathrm{L}$, the scanned area on the ground $A_\mathrm{L} = L_\mathrm{v}\,L_\mathrm{h} = 4\,d_\mathrm{t}\,\tan\left(\gamma_\mathrm{v}/2\right)\,\tan\left(\gamma_\mathrm{h}^*/2\right)$ with the valid horizontal field of view γ_h^* and $d_\mathrm{t} = |z_\mathrm{t} - z|$ has to be considered. The number of measurement points is then given by $N_\mathrm{p} = (\gamma_\mathrm{v}\,\gamma_\mathrm{h}^*)/(V_\mathrm{res}\,H_\mathrm{res})$. Ensuring a minimum point cloud density $R_\mathrm{L,min}$, the distance d_t must satisfy

$$d_\mathrm{t} \leq \sqrt{\frac{\gamma_\mathrm{v}\,\gamma_\mathrm{h}^*}{4\,R_\mathrm{L,min}\,\tan\left(\gamma_\mathrm{v}/2\right)\,\tan\left(\gamma_\mathrm{h}^*/2\right)}},$$

while $d_\mathrm{t} \leq r_\mathrm{L}\,\cos\left(\gamma_\mathrm{v}/2\right)$ and $d_\mathrm{t} \leq r_\mathrm{L}\,\cos\left(\gamma_\mathrm{h}^*/2\right)$ ensure valid measurements. Further, the UAV's ground velocity v_g is constrained by

$$v_\mathrm{g} \leq 2\,|z_\mathrm{t} - z|\,\tan\left(\gamma_\mathrm{v}/2\right)\,\left(1-\delta_\mathrm{c}\right)f_\mathrm{L},$$

where $\delta_\mathrm{L} \in [0,1]$ is the overlap of successive scans and f_L is the scanning rate.

For the second LiDAR configuration, the sensor is mounted to scan the horizontal plane with its rotation axis aligned with the UAV's z^B-axis, as shown in Fig. 8b. This configuration is typically used for obstacle detection, requiring the UAV to limit its ground velocity so that it can react in time to detected obstacles. The ground velocity v_g must satisfy

$$v_\mathrm{g} \leq -a_\mathrm{B,max}\,t_\mathrm{R} + \sqrt{\left(a_\mathrm{B,max}\,t_\mathrm{R}\right)^2 + r_\mathrm{L}},$$

where t_{R} is the detection time and $a_{\mathrm{B,max}}$ is the maximum braking acceleration, approximated by $a_{\mathrm{B,max}} \approx \alpha_{\max}\mathrm{g}$. Additionally, the tilt angle α should be constrained by the LiDAR's vertical field of view γ_{v} to maintain a clear detection of obstacles in front of the UAV, with

$$\alpha \leq \gamma_{\mathrm{v}}/2.$$

V. Energy Aware Multicopter Model

The derived multicopter and energy consumption models are combined, as illustrated in Fig. 9, to obtain the discrete-time NPV energy-aware multicopter model

$$\begin{aligned}\dot{\mathbf{x}} &= \mathbf{f}(\mathbf{x},\mathbf{u}) + \boldsymbol{\Gamma}_{\mathrm{x}} = \begin{pmatrix}\mathbf{f}_{\mathrm{u}}\left(\mathbf{x}_{\mathrm{u}},\mathbf{f}_{\mathrm{c}}(\mathbf{u})\right)\\ \mathbf{f}_{\mathrm{e}}\left(\mathbf{x}_{\mathrm{e}},\mathbf{u}\right)\end{pmatrix} + \begin{pmatrix}\boldsymbol{\Gamma}_{\mathrm{u,x}}\\ \boldsymbol{\Gamma}_{\mathrm{e,x}}\end{pmatrix},\\ \mathbf{y} &= \mathbf{g}(\mathbf{x},\mathbf{u}) + \boldsymbol{\Gamma}_{\mathrm{y}} = \mathbf{g}_{\mathrm{e}}(\mathbf{x}_{\mathrm{e}},\mathbf{u}) + \boldsymbol{\Gamma}_{\mathrm{e,y}},\end{aligned}$$

with the state $\mathbf{x} = (\mathbf{x}_{\mathrm{u}}^{\top}, \mathbf{x}_{\mathrm{e}}^{\top})^{\top}$, the input $\mathbf{u} = (\Omega_1, \ldots, \Omega_{N_{\mathrm{M}}})^{\top}$ and the output $\mathbf{y} = \mathbf{y}_{\mathrm{e}}$. The transformation $\mathbf{u}_{\mathrm{u}} = \mathbf{f}_{\mathrm{c}}(\mathbf{u})$ of the input $\mathbf{u}$ into the input $\mathbf{u}_{\mathrm{u}}$ of the nonlinear multicopter model (4) is derived in (9) and (10).

Meanwhile, the discrete-time LPV energy aware multicopter model with the reduced input $\tilde{\mathbf{u}} = (\tilde{\mathbf{u}}_{\mathrm{u}}^{\top}, \tilde{\mathbf{u}}_{\mathrm{e}}^{\top})^{\top}$ is given by

$$\begin{aligned}\mathbf{x}(k+1) &= \mathbf{A}_{\mathrm{d}}\mathbf{x}(k) + \mathbf{B}_{\mathrm{d}}\tilde{\mathbf{u}}(k) + \mathbf{E}_{\mathrm{d}} + \boldsymbol{\Gamma}_{\mathrm{x}},\\ \mathbf{y}(k) &= \mathbf{C}_{\mathrm{d}}\mathbf{x}(k) + \mathbf{D}_{\mathrm{d}}\tilde{\mathbf{u}}(k) + \mathbf{y}_{\mathrm{SP}} + \boldsymbol{\Gamma}_{\mathrm{y}}.\end{aligned}$$

It comprises the discrete-time state-space matrices

$$\begin{aligned}\mathbf{A}_{\mathrm{d}} &= \begin{bmatrix}\mathbf{A}_{\mathrm{d,u}} & \mathbf{0}\\ \mathbf{0} & \mathbf{A}_{\mathrm{d,e}}\end{bmatrix}, \quad \mathbf{B}_{\mathrm{d}} = \begin{bmatrix}\mathbf{B}_{\mathrm{d,u}} & \mathbf{0}\\ \mathbf{0} & \mathbf{B}_{\mathrm{d,e}}\end{bmatrix}, \quad \mathbf{E}_{\mathrm{d}} = \begin{bmatrix}\mathbf{0}\\ \mathbf{E}_{\mathrm{d,e}}\end{bmatrix},\\ \mathbf{C}_{\mathrm{d}} &= \begin{bmatrix}\mathbf{0} & \mathbf{C}_{\mathrm{d,e}}\end{bmatrix}, \qquad \mathbf{D}_{\mathrm{d}} = \begin{bmatrix}\mathbf{0} & \mathbf{D}_{\mathrm{d,e}}\end{bmatrix}.\end{aligned}$$

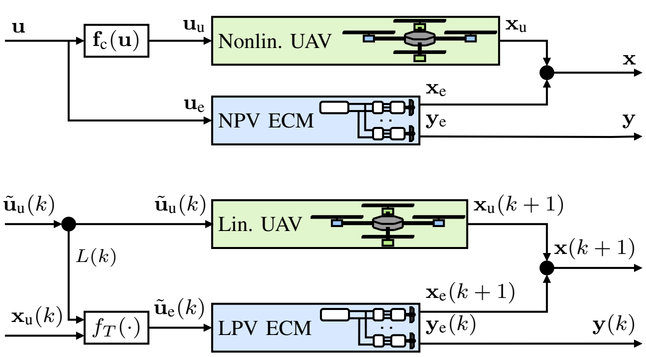

Fig. 9. Structure of the nonlinear (top) and linear (bottom) energy aware multicopter model

The separation of the inputs for the multicopter model and the ECM allows for considering aerodynamic effects that are not included in the linear multicopter model. Since the horizontal and vertical motion dynamics are not coupled, we correct the necessary thrust during tilted flight by

$$\Delta T = \sqrt{T_{\mathrm{v}}^2 + T_{\mathrm{h}}^2} - T_{\eta} - T_{\mathrm{SP}}. \tag{24}$$

Here, $T_{\mathrm{v}} = T\cos(\alpha) = T_{\mathrm{SP}} + L$ is the vertical thrust component and $T_{\mathrm{h}} = T\sin(\alpha) \approx m\,\mathrm{g}\,\alpha$ is the horizontal thrust component. It is observed that a small-size multicopter in forward flight consumes equal or even less power compared to hovering until a threshold velocity is reached [6, 39]. This is the result of multiple rotor efficiency increasing aerodynamic effects, such as the increased air inflow velocity through the rotors or the effective translational lift [1, 40]. Due to the nonlinear and difficult-to-model nature of these effects, we approximate the increased efficiency by reducing the necessary thrust for velocities below the threshold v_{th} by

$$T_{\eta} = \begin{cases}\frac{\eta_{\mathrm{ETL}}\, m\, \mathrm{g}}{v_{\mathrm{th}}}\, v_{\mathrm{g}} & \text{for } v_{\mathrm{g}} \leq v_{\mathrm{th}},\\ \eta_{\mathrm{ETL}}\, m\, \mathrm{g} & \text{for } v_{\mathrm{g}} \geq v_{\mathrm{th}}.\end{cases}$$

Here, $\eta_{\mathrm{ETL}} = \sqrt{1 + \left(\frac{c_{\mathrm{F}}\, v_{\mathrm{th}}}{m\, \mathrm{g}}\right)^2} - 1$ results in an equal power consumption for hovering and for steady horizontal flight with $v_{\mathrm{g}} = v_{\mathrm{th}}$.

Accurately representing the vehicle's capabilities, the constraints outlined in Sections II-E and III-E must be satisfied. Further, if the UAV is equipped with a sensor the constraints in Section IV must be considered during measurements.

Remark 6. *For the parameter identification the masses of the UAV, battery and equipment has to be summed up to the total mass* m*. Additionally, the inertia tensor* $\mathbf{J}$ *must be adjusted regarding the battery and equipment, preferring to be attached close to the UAV's body.*

VI. Discussion

In the following, we discuss the modeling of the UAVs and their energy consumption,and validate them by actual test flight data.

A. Multicopter Model

In Section II, we derived a multicopter model (4) that is suitable for UAS swarms with various UAVs because it is easily adaptable to fit all sorts of multicopter configurations. However, the models have their limitations in terms of accuracy. We employ Assumption 3 for the aerodynamic parameters k_{F} and k_{M}, which we define for the hovering state (no external airflow, constant motor speeds). This leads to an estimation error for the aerodynamic forces and torques. In addition, the models have no upper limit for their flight altitude, since the aerodynamic parameters do not decrease depending on the air pressure. Additional aerodynamic effects such as the effective translational lift or the dynamic air inflow of the rotors, should be considered to improve the accuracy [40]. The approximations on the dynamics and parameters result in uncertainties, which should be considered for path planning to ensure that the paths are safe and will not lead to collisions. Unfortunately, these are impossible to predict and only can be partly modeled. Furthermore, the mapping between the inputs of the linear multicopter model (5) to the motor speeds is only valid under the condition outlined in Remark 2.

B. Energy Consumption Models

In Section III, we derived an ECM (22) that is easily adaptable to different electric-propelled UAVs. To validate the ECM and the individual component models, we identify the model parameters of a "Holybro S500 V2", which are listed in Appendix C. Some parameters are taken directly from data sheets, other unknown parameters are fitted using the *greyest* algorithm in Matlab, see [38], and data from a calibration flight (TD), recorded by the Pixhawk autopilot [34]. The models are validated with measurements from additional test flights, which are defined in Appendix D.

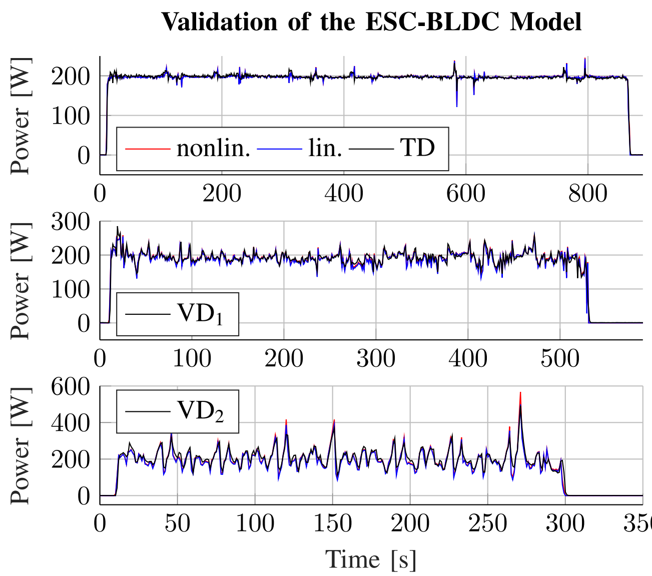

Fig. 10. Supply Power estimation of the nonlinear (red) and linear (blue) ESC-BLDC models, compared to measurements (black) of actual test flights

Fig. 10 shows the combined supply power estimation of all four BLDC motors for the nonlinear and linearized ESC-BLDC model. It turns out, that the supply power is estimated adequately during flight. However, the nonlinear model overestimates the supply power at high motor speeds. This behavior results from Assumption 3 in (20), since the supply power increases with the fourth power of Ω, which is actual damped by a decreasing k_{M}. It also shows that the linearized model often underestimates the power consumption slightly for motor speeds below the set point.

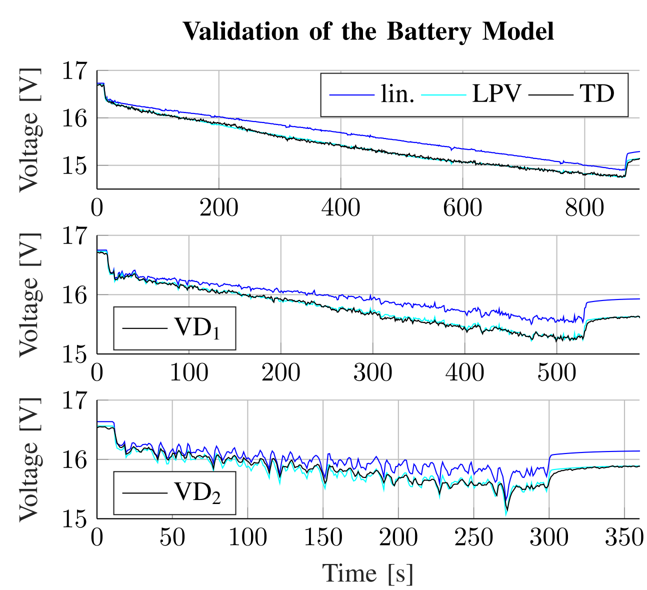

Fig. 11. Battery voltage estimation of the linear (blue) and LPV (cyan) battery models, compared to measurements (black) of actual test flights

Fig. 11 shows the battery voltage estimation of the battery model (14) employing a linear and a LPV Thevenin model as LIB cells. The LPV battery model estimates the battery voltage with high accuracy. However, the estimation error increases during the relaxation phase. This is a known characteristic of the Thevenin model and is solved by the Dual-Polarization Model, which uses an additional RC-network in series to represent different polarization effects [16, 30].

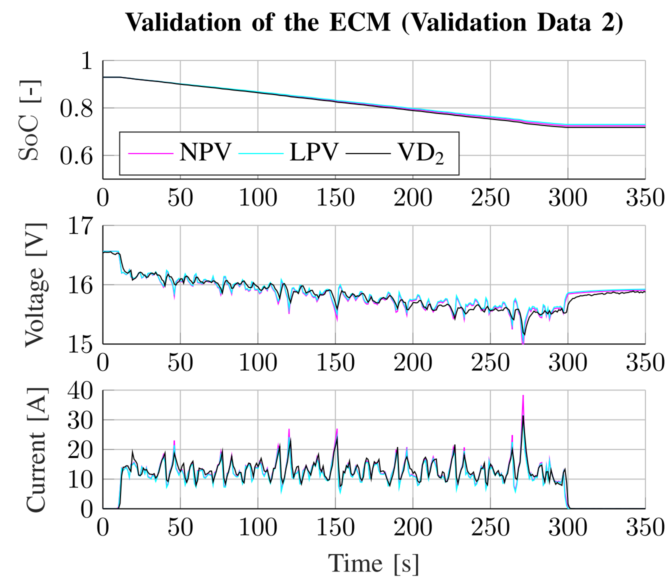

Fig. 12. Energy consumption estimation of the NPV (magenta) and LPV (cyan) ECMs, compared to measurements (black) of validation test flight VD$_2$

To validate the combined ECM, the energy consumption estimates of several ECM formulations are compared with the measurements from the test flights. As an example, Fig. 12 shows the battery state measurements and estimates using the NPV and LPV ECMs for the second validation test flight. While both models slightly underestimate the energy consumption, the NPV ECMs show better estimation results than the LPV ECMs due to the overestimated supply power of the ESC-BLDC model. All ECMs show the same estimation errors for the relaxing phase as their corresponding battery models. As metric for comparison, we use the state of charge estimation error $f_{\mathrm{error}} = |\Delta\mathrm{SoC} - \Delta\tilde{\mathrm{SoC}}| \cdot 100\%$, where $\Delta\mathrm{SoC}$ and $\Delta\tilde{\mathrm{SoC}}$ are the actual and estimated differences in the state of charge change SoC after five minutes of flight.

TABLE I
STATE OF CHARGE ESTIMATION ERRORS AFTER FIVE MINUTES.

	nonlin.	NPV	lin.	LPV
TD	0.40%	0.22%	0.46%	0.29%
VD$_1$	0.34%	0.18%	0.55%	0.39%
VD$_2$	0.89%	0.66%	1.46%	1.25%

As shown in Tab. I, the ECMs can accurately estimate the state of charge, and the estimation errors are less than 2% even for flight profiles that deviate significantly from the set point. Furthermore, parameter-varying variants of the ECMs can improve the estimation accuracy. The ECMs show a self-amplifying effect for the estimation errors, which is present in the simulation because we use do not correct the state estimations by actual measurements.

C. Energy Aware Multicopter Model in Path Planning

In [14], the developed discrete-time linear energy aware multicopter model and the parameters of the "Holybro S500 V2", are implemented in an online moving horizon path planning algorithm to plan energy efficient paths for a UAS swarm on a search and rescue mission, resulting in the flight paths drawn in Fig. 13. Additionally, Fig. 14 illustrates the results of the energy consumption simulation of the two UAVs. Note, that UAV 2 is already partly discharged at the beginning of the mission and returns during the mission to its base, where it lands and deactivates itself.

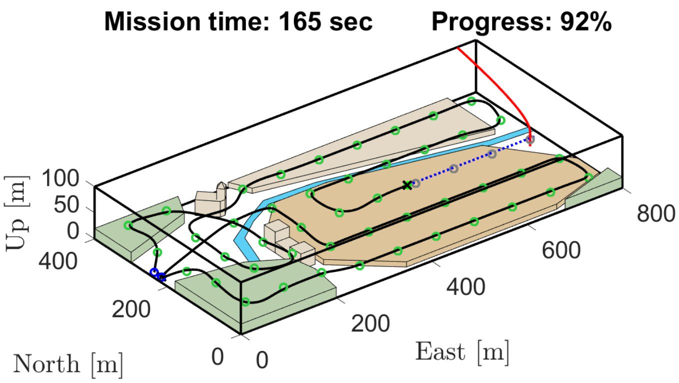

Fig. 13. UAS swarm on a search-and-rescue mission in a small flooded village employing two UAVs to autonomously cover the search area; UAV: position (black cross), past path (black line), planned path (blue dots); Moving obstacle (e.g. a rescue helicopter): past path (red line) [14]

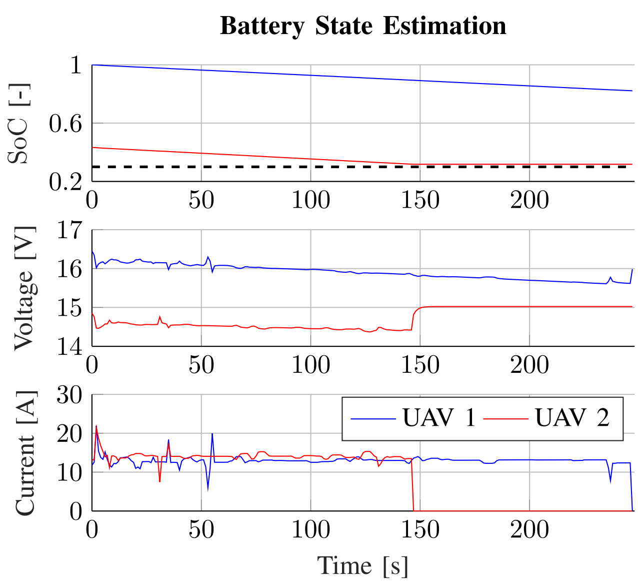

Fig. 14. Energy consumption simulation for two UAVs [14]

The state of charge, the battery voltage and the battery current of UAV 1 and UAV 2 are shown in blue and red, respectively. It can be seen that UAV 2 is drawing a higher current to compensate for its lower charge and battery voltage. The ECM can reproduce the desired effects that affect the energy consumption. It increases when climbing, turning, braking, or accelerating and decreases when descending. Due to (24) the power consumption during horizontal flight at maximum velocity is only slightly higher, compared to a steady hover flight, which also is observable in reality.

VII. Conclusion

In this study, we developed a modular modeling approach for multicopter UAVs, with a focus on their energy consumption and applicability to control and planning applications.

We derived an adaptable multicopter model capable of representing a wide range of multicopter configurations, making it suitable for heterogeneous UAS swarms. In doing so, we incorporated important factors such as vehicle capabilities, external disturbances, and uncertainties to ensure the model closely represents real-world flight dynamics. Moreover, we derived an ECM for electric-propelled UAVs. By adopting a component-based modeling approach, the detailed model design enables us to consider different UAV designs, enhancing the adaptability of the model. A scheme for an electric-propelled UAV's power train was designed, consisting of BLDC motors (modeled as simplified direct current motors), ESCs (modeled as DC-DC-converters), and LIBs (modeled as networks of LIB cells employing an equivalent circuit design approach). Together, these components form the ECM, which allows for accurate estimation of the battery state based on motor speeds and power demands from additional subsystems, like the avionics or the payload. This approach ensures adaptability across a wide range of electric-propelled UAVs. The combined nonlinear model was further linearized and discretized for a multicopterUAV, making it suitable for integration into control and planning algorithms. This is demonstrated by its use in the path planner developed in the companion study. In addition, sensor models for camera and LiDAR systems were derived, offering the flexibility to integrate mission-specific constraints and sensor limitations into the planning process.

Overall, this modular approach provides a solid foundation for detailed analysis and optimization of multicopter UAV operations, enabling more precise control and mission execution under real-world conditions.

Appendix A
Discrete-time Linear State Space Models

We linerize the nonlinear models (4) and (22) around the hovering state with a fully charged battery

$$
\begin{aligned}
\mathbf{x}_{\text{u,SP}} &= (0,\dots,0)^\top, & \mathbf{x}_{\text{e,SP}} &= (0,0)^\top,\\
\mathbf{u}_{\text{u,SP}} &= (T_{\text{SP}},0,0,0,0)^\top, & \mathbf{u}_{\text{e,SP}} &= (\Omega_{\text{SP}},\dots,\Omega_{\text{SP}})^\top,\\
\mathbf{d}_{\text{u,SP}} &= (0,\dots,0)^\top,
\end{aligned}
$$

wherein the multicopter maintains its position while the thrust $T_{\text{SP}} = m\,g$ compensates for the weight force, resulting in motor speeds of $\Omega_{\text{SP}} = \sqrt{\frac{m\,g}{N_{\text{M}}\,k_{\text{F}}}}$. In the following uncertainties are not considered.

Remark 7. *In linearized models, deviations from the set point are used. For example, the state deviation $\Delta\mathbf{x}$ is defined as $\Delta\mathbf{x} = \mathbf{x} - \mathbf{x}_{SP}$. However, when the variable is 0 at the set point, Δ is omitted for clarity.*

A. Discrete-time Linear Multicopter Model

For the multicopter model, this set point is an equilibrium point and the linear model is given by

$$\dot{\mathbf{x}}_\mathrm{u} = \mathbf{f}_\mathrm{u,lin}(\mathbf{x}_\mathrm{u}, \tilde{\mathbf{u}}_\mathrm{u}, \mathbf{d}_\mathrm{u})$$

$$= \begin{pmatrix} v_\mathrm{x} \\ v_\mathrm{y} \\ v_\mathrm{z} \\ -\mathrm{g}\,(\theta\,\cos(\psi_\mathrm{SP}) + \phi\,\sin(\psi_\mathrm{SP})) - c_\mathrm{Fx}\,(v_\mathrm{x} - v_\mathrm{w,x})/m \\ -\mathrm{g}\,(\theta\,\sin(\psi_\mathrm{SP}) - \phi\,\cos(\psi_\mathrm{SP})) - c_\mathrm{Fy}\,(v_\mathrm{y} - v_\mathrm{w,y})/m \\ -L/m - c_\mathrm{Fz}\,(v_\mathrm{z} - v_\mathrm{w,z})/m \\ \omega_\mathrm{x} \\ \omega_\mathrm{y} \\ \omega_\mathrm{z} \\ (\tau_\mathrm{x} - \omega_\mathrm{x}\,c_{\tau\mathrm{x}})/J_\mathrm{xx} \\ (\tau_\mathrm{y} - \omega_\mathrm{y}\,c_{\tau\mathrm{y}})/J_\mathrm{yy} \\ (\tau_\mathrm{z} - \omega_\mathrm{z}\,c_{\tau\mathrm{z}})/J_\mathrm{zz} \end{pmatrix}.$$

For $\psi_\mathrm{SP} = 0$, the transformation matrices $\mathbf{R}_\mathrm{B}^\mathrm{I}$ and $\mathbf{R}_\Psi^{-1}$ equal identity matrices, resulting in a direct transformation of vectors and rotation rates between the body-fixed and inertial frame. Therefore, the alignment of the x^B- and y^B-axis is not affected by the yaw angle ψ anymore. Likewise, the alignment of the z^B-axis is not affected by the roll and pitch angels ϕ, θ. Since the thrust T now only acts in negative z^I-direction, we replace it with the lift $L \approx T - T_\mathrm{SP}$. Further, the difference in rotor speeds Ω_r, defined by (6), does not affect the dynamics anymore, so we reduce the input to

$$\tilde{\mathbf{u}}_\mathrm{u} = (L, \tau_\mathrm{x}, \tau_\mathrm{y}, \tau_\mathrm{z})^\top.$$

This linear model is discretized with a sampling time of Δt using Taylor-Lie series, as described in Appendix B. In order to more accurately approximate the discrete-time model a discretization order $N_\mathrm{dis} \geq 2$ is recommended due to the high dynamics of the multicopter. Finally, the discrete-time linear state-space multicopter model is given by

$$\mathbf{x}_\mathrm{u}(k+1) = \mathbf{A}_\mathrm{d,u}\,\mathbf{x}_\mathrm{u}(k) + \mathbf{B}_\mathrm{d,u}\,\tilde{\mathbf{u}}_\mathrm{u}(k) + \mathbf{H}_\mathrm{d,u}\,\mathbf{d}_\mathrm{u}(k),$$

where $\mathbf{A}_\mathrm{d,u}$, $\mathbf{B}_\mathrm{d,u}$ and $\mathbf{H}_\mathrm{d,u}$ are the discrete-time system, input and disturbance matrices.

B. Discrete-time Linear Energy Consumption Model

We start with the already linear LIB equations (14)

$$\begin{aligned} \dot{\mathbf{x}}_\mathrm{b} &= \mathbf{A}_\mathrm{b}\,\mathbf{x}_\mathrm{b} + \mathbf{B}_\mathrm{b}\,\mathbf{u}_\mathrm{b}, \\ \mathbf{y}_\mathrm{b} &= \mathbf{C}_\mathrm{b}\,\mathbf{x}_\mathrm{b} + \mathbf{D}_\mathrm{b}\,\mathbf{u}_\mathrm{b}, \end{aligned}$$

with the battery state $\mathbf{x}_\mathrm{b} = (\mathrm{DoD}, u_\mathrm{th})^\top$, input $\mathbf{u}_\mathrm{b} = i_\mathrm{b}$ and output $\mathbf{y}_\mathrm{b} = (\mathrm{SoC}, u_\mathrm{b}, i_\mathrm{b})^\top$, and the state-space matrices

$$\mathbf{A}_\mathrm{b} = \begin{bmatrix} 0 & 0 \\ 0 & -1/(R_\mathrm{th}\,C_\mathrm{th}) \end{bmatrix}, \qquad \mathbf{B}_\mathrm{b} = \begin{bmatrix} \eta_\mathrm{b}/Q_\mathrm{b} \\ 1/(N_\mathrm{P}\,C_\mathrm{th}) \end{bmatrix},$$

$$\mathbf{C}_\mathrm{b} = \begin{bmatrix} -1 & 0 \\ N_\mathrm{S}\,b_1 & -N_\mathrm{S} \\ 0 & 0 \end{bmatrix}, \qquad \mathbf{D}_\mathrm{b} = \begin{bmatrix} 0 \\ -(N_\mathrm{S}\,R_\mathrm{int})/N_\mathrm{P} \\ 1 \end{bmatrix}.$$

Next, we derive from (20) a linear approximation of the power consumption of a BLDC motor

$$\Delta p_\mathrm{DC} = \left.\frac{\mathrm{d}p_\mathrm{DC}}{\mathrm{d}\Omega^2}\right|_\mathrm{SP} \Delta\Omega^2 = \kappa_\mathrm{DC}\,\Delta\Omega^2$$

depending on the motor speed squared around the set point, where κ_DC substitutes for

$$\kappa_\mathrm{DC} = K_\mathrm{V}^2\,R_\mathrm{DC}(2\,k_\mathrm{M}^2\,\Omega_\mathrm{SP}^2 + 3\,k_\mathrm{M}\,D_\mathrm{f}\,\Omega_\mathrm{SP} + D_\mathrm{f}^2) + \frac{3}{2}\,k_\mathrm{M}\,\Omega_\mathrm{SP} + D_\mathrm{f}.$$

Combining all BLDC motors together, while considering (9) and Assumption 2, we formulate the total power consumption of the BLDC motors $p_{\mathrm{DC},\Sigma}$ depending on the thrust T by

$$\Delta p_\Sigma = \sum_{i=1}^{N_\mathrm{M}} \Delta p_\mathrm{DC} = \frac{\kappa_\mathrm{DC}}{k_\mathrm{F}}\,\Delta T,$$

The power consumption of the BLDC motors during hovering

$$\begin{aligned} &p_\mathrm{DC,SP} = R_\mathrm{DC}\,K_\mathrm{V}^2\,\left(D_\mathrm{f}\,\Omega_\mathrm{SP} + k_\mathrm{M}\,\Omega_\mathrm{SP}^2\right)^2 + D_\mathrm{f}\,\Omega_\mathrm{SP}^2 + k_\mathrm{M}\,\Omega_\mathrm{SP}^3, \\ &p_{\Sigma,\mathrm{SP}} = N_\mathrm{M}\,p_\mathrm{DC,SP} \end{aligned}$$

is calculated by (20).

To connect the BLDC motors with the battery, we derive from (21) the linear approximation for the current i_b drawn from the battery by the ESCs:

$$\Delta i_\mathrm{b} = \sum_{i=1}^{N_\mathrm{M}} \Delta i_{\mathrm{ESC},i} = \kappa_\mathrm{DoD}\mathrm{DoD} + \kappa_\mathrm{uth} u_\mathrm{th} + \kappa_\mathrm{p}\Delta p_\Sigma,$$

where κ_DoD, κ_uth and κ_p substitute for

$$\kappa_\mathrm{DoD} = \frac{N_\mathrm{P}\,b_1}{2\,R_\mathrm{int}}(1-\kappa), \qquad \kappa_\mathrm{uth} = \frac{N_\mathrm{P}}{2\,R_\mathrm{int}}(\kappa - 1),$$

$$\kappa_\mathrm{p} = \frac{\kappa}{N_\mathrm{S}\,b_0\,\eta_\mathrm{ESC}}, \qquad \kappa^{-1} = \sqrt{1 - \frac{4\,R_\mathrm{int}}{N_\mathrm{S}\,N_\mathrm{P}\,b_0^2\,\eta_\mathrm{ESC}} p_{\Sigma,\mathrm{SP}}}.$$

From (20) and (21), we derive the current draw from the battery during hovering

$$i_\mathrm{b,SP} = \frac{N_\mathrm{P}\,b_0}{2\,R_\mathrm{int}}\left(1 - \kappa^{-1}\right).$$

Finally, we define for the linear multicopter ECM, the state $\mathbf{x}_\mathrm{e} = \mathbf{x}_\mathrm{b}(\mathrm{DoD}, u_\mathrm{th})^\top$, the input $\tilde{\mathbf{u}}_\mathrm{e} = \Delta T$ and the output $\mathbf{y}_\mathrm{e} = \mathbf{y}_\mathrm{b} = (\mathrm{SoC}, u_\mathrm{b}, i_\mathrm{b})^\top$, which is $\mathbf{y}_\mathrm{e,SP} = \mathbf{D}_\mathrm{b}\,i_\mathrm{b,SP}$ at the set point. Combining all components of the power train, the linear ECM is given by

$$\begin{aligned} \dot{\mathbf{x}}_\mathrm{e} &= \mathbf{f}_\mathrm{e,lin}(\mathbf{x}_\mathrm{e}, \tilde{\mathbf{u}}_\mathrm{e}) = \mathbf{A}_\mathrm{e}\,\mathbf{x}_\mathrm{e} + \mathbf{B}_\mathrm{e}\,\tilde{\mathbf{u}}_\mathrm{e} + \mathbf{E}_\mathrm{e}, \\ \mathbf{y}_\mathrm{e} &= \mathbf{g}_\mathrm{e,lin}(\mathbf{x}_\mathrm{e}, \tilde{\mathbf{u}}_\mathrm{e}) = \mathbf{C}_\mathrm{e}\,\mathbf{x}_\mathrm{e} + \mathbf{D}_\mathrm{e}\,\tilde{\mathbf{u}}_\mathrm{e} + \mathbf{y}_\mathrm{e,SP}, \end{aligned}$$

with the state-space matrices

$$\mathbf{A}_\mathrm{e} = \mathbf{A}_\mathrm{b} + \mathbf{B}_\mathrm{b}\left(\kappa_\mathrm{DoD} \quad \kappa_\mathrm{uth}\right), \quad \mathbf{B}_\mathrm{e} = \mathbf{B}_\mathrm{b}\,\frac{\kappa_\mathrm{p}\,\kappa_\mathrm{DC}}{k_\mathrm{F}},$$

$$\mathbf{C}_\mathrm{e} = \mathbf{C}_\mathrm{b} + \mathbf{D}_\mathrm{b}\left(\kappa_\mathrm{DoD} \quad \kappa_\mathrm{uth}\right), \quad \mathbf{D}_\mathrm{e} = \mathbf{D}_\mathrm{b}\,\frac{\kappa_\mathrm{p}\,\kappa_\mathrm{DC}}{k_\mathrm{F}}.$$

Since the set point is not an equilibrium point, we add

$$\mathbf{E}_\mathrm{e} = \mathbf{B}_\mathrm{b}\,i_\mathrm{b,SP}$$

as an offset for the energy consumption during hovering.

This linear model is discretized with a sampling time of Δt using Taylor series, since a discretization order $N_{\text{dis}} = 1$ is sufficient due to the direct influence of the input on the state. Then, the discrete-time linear state-space ECM is given by

$$\begin{aligned}\mathbf{x}_{\text{e}}(k+1) &= \mathbf{A}_{\text{d,e}}\,\mathbf{x}_{\text{e}}(k) + \mathbf{B}_{\text{d,e}}\,\tilde{\mathbf{u}}_{\text{e}}(k) + \mathbf{E}_{\text{d,e}},\\ \mathbf{y}_{\text{e}}(k) &= \mathbf{C}_{\text{d,e}}\,\mathbf{x}_{\text{e}}(k) + \mathbf{D}_{\text{d,e}}\,\tilde{\mathbf{u}}_{\text{e}}(k) + \mathbf{y}_{\text{e,SP}},\end{aligned}$$

with the discrete-time system, input and disturbance matrices

$$\begin{aligned}&\mathbf{A}_{\text{d,e}} = \mathbf{I} + \mathbf{A}_{\text{e}}\Delta t, \quad \mathbf{B}_{\text{d,e}} = \mathbf{B}_{\text{e}}, \quad \mathbf{E}_{\text{d,e}} = \mathbf{E}_{\text{e}}\Delta t,\\ &\mathbf{C}_{\text{d,e}} = \mathbf{C}_{\text{e}}, \qquad\qquad \mathbf{D}_{\text{d,e}} = \mathbf{D}_{\text{e}}.\end{aligned}$$

Remark 8. *Here, the parameters b_0 and b_1 can be ether selected according to (15) or (16) for the linear or LPV ECM.*

APPENDIX B
DISCRETIZATION USING TAYLOR-LIE SERIES

For discretizations, we adopt Lie-derivatives

$$\begin{aligned}L_{\mathbf{f}}^1\,\mathbf{f}(t,\mathbf{x},\mathbf{u},\mathbf{d}) =& \frac{\partial\,\mathbf{f}}{\partial\,t}(t,\mathbf{x},\mathbf{u},\mathbf{d})\ldots\\ &+ \nabla_{\mathbf{x}}\,\mathbf{f}(t,\mathbf{x},\mathbf{u},\mathbf{d})\cdot\mathbf{f}(t,\mathbf{x},\mathbf{u},\mathbf{d}),\\ L_{\mathbf{f}}^k\,\mathbf{f}(t,\mathbf{x},\mathbf{u},\mathbf{d}) =& \frac{\partial\left(L_{\mathbf{f}}^{k-1}\,\mathbf{f}\right)}{\partial\,t}(t,\mathbf{x},\mathbf{u},\mathbf{d})\ldots\\ &+ \nabla_{\mathbf{x}}\left(L_{\mathbf{f}}^{k-1}\,\mathbf{f}\right)(t,\mathbf{x},\mathbf{u},\mathbf{d})\cdot\mathbf{f}(t,\mathbf{x},\mathbf{u},\mathbf{d}),\end{aligned}$$

to increase the accuracy of the discrete-time system dynamics approximation. Then, the discrete-time model is described by

$$\begin{aligned}\mathbf{x}(k+1) = \mathbf{f}_{\text{d}}(t,\mathbf{x},\mathbf{u},\mathbf{d},\Delta t) &= \mathbf{x} + \mathbf{f}(t,\mathbf{x},\mathbf{u},\mathbf{d})\cdot\Delta t\\ &+ \sum_{k=2}^{N_{\text{dis}}} L_{\mathbf{f}}^{k-1}\,\mathbf{f}(t,\mathbf{x},\mathbf{u},\mathbf{d})\cdot\frac{\Delta t^k}{k!},\end{aligned}$$

where Δt is a constant sampling time, and N_{dis} is the discretization degree [18].

APPENDIX C
MODEL PARAMETERS

TABLE II
VEHICLE PARAMETERS AND LIMITATIONS

Quadcopter "Holybro S500 V2" (with battery)

$m = 1.45\,\text{kg}$	$\ell = 0.24\,\text{m}$	$J_{\text{xx}} = J_{\text{yy}} = 0.0158\,\text{kg}\,\text{m}^2$
$N_{\text{M}} = 4$	$v_{\text{th}} = 10\,\text{m/s}$	$J_{\text{zz}} = 0.0252\,\text{kg}\,\text{m}^2$
$v_{\max} = 13.5\,\text{m/s}$	$v_{\text{z,max}} = 5\,\text{m/s}$	$\delta_{\text{UAS}} = 0.37\text{m}$
$\alpha_{\max} = 30°$	$\omega_{\max} = 15°/\text{s}$	$c_{\text{F},i} = 0.27\,(\text{N}\,\text{s})/\text{m}$
$l_{\text{x},i} = l_{\text{y},i} = \sqrt{2}/2\,\ell = 0.17\,\text{m}$		$c_{\tau,i} = 0.1\,(\text{N}\,\text{m}\,\text{s})/\text{rad}$

ESC "BLHeli-S 20A" & BLDC "AIR2216II" & Rotor "T1045II"

$R_{\text{DC}} = 57.5\,\text{m}\Omega$	$k_{\text{F}} = 1.21\cdot 10^{-5}\,\text{N}/(\text{rad/s})^2$
$K_{\text{V}} = 96.34\,(\text{rad/s})/\text{V}$	$k_{\text{M}} = 1.74\cdot 10^{-7}\,\text{Nm}/(\text{rad/s})^2$
$\Omega_{\max} = 1032\,\text{rad/s}$	$J_{\text{r}} = 9.86\cdot 10^{-5}\,\text{kg}\,\text{m}^2$
$u_{\text{DC,norm}} = 16\,\text{V}$	$\eta_{\text{ESC}} = 0.86$

LIB "Gens Ace B-50C-5000-4S1P-Bashing"

$N_{\text{S}} = 4$, $N_{\text{P}} = 1$	$Q_{\text{b}} = 18000\,\text{As}$	$\eta_{\text{b}} = 1$
$R_{\text{int}} = 6.62\,\text{m}\Omega$	$R_{\text{th}} = 1.56\,\text{m}\Omega$	$C_{\text{th}} = 15.6\,\text{kF}$
$u_{\text{c,min}} = 2.75\,\text{A}$	$u_{\text{c,max}} = 4.2\,\text{A}$	$i_{\text{discharge,max}} = 250\,\text{A}$
$u_{\text{b,norm}} = 14.8\,\text{V}$	$\text{DoD}_{\text{cutoff}} = 0.85$	$\text{DoD}_{\max} = 0.7$
$b_0 = 4.2\,\text{V}$	$b_1 = -0.5765\,\text{V}$	$\overline{\text{DoD}}_0 = 0$
$b_{0,1} = 4.2\,\text{V}$	$b_{1,1} = -0.8395\,\text{V}$	$\overline{\text{DoD}}_1 = 0.2$
$b_{0,2} = 4.1727\,\text{V}$	$b_{1,2} = -0.7028\,\text{V}$	$\overline{\text{DoD}}_2 = 0.4$
$b_{0,3} = 4.0529\,\text{V}$	$b_{1,3} = -0.4034\,\text{V}$	$\overline{\text{DoD}}_3 = 0.9$

APPENDIX D
TEST FLIGHTS WITH A "HOLYBRO S500 V2"

- Trainings Data (TD): hovering with frequently impulsive changes in altitude; indoors
- Validation Data 1 (VD_1): rectangle trajectory following; medium cruise velocity ($v_{\text{cruise}} = 19\text{km/h}$); outdoors
- Validation Data 2 (VD_2): rectangle trajectory following; high cruise velocity ($v_{\text{cruise}} = 43\text{km/h}$); outdoors

Remark 9. *The flight profile of the validation test flights does not represent a horizontal flight because the autopilot could not maintain altitude during braking or acceleration.*

REFERENCES

[1] Federal Aviation Administration. *Helicopter flying handbook (FAA-H-8083-21B)*. Skyhorse Publishing, 2019.

[2] S. Ali, T. Abuhmed, S. El-Sappagh, K. Muhammad, J. Alonso, R. Confalonieri, R. Guidotti, J. Del Ser, N. Díaz-Rodríguez, and F. Herrera. Explainable artificial intelligence (xai): What we know and what is left to attain trustworthy artificial intelligence. *Information Fusion*, 99:101805, 04 2023.

[3] R. Alyassi, M. Khonji, A. Karapetyan, S. C. Chau, K. Elbassioni, and C. Tseng. Autonomous recharging and flight mission planning for battery-operated autonomous drones. *IEEE Transactions on Automation Science and Engineering*, 20(2): 1034–1046, 2023.

[4] I. Asti, T. Agustinah, and A. Santoso. Obstacle avoidance with energy efficiency and distance deviation using knn algorithm for quadcopter. In *2020 International Seminar on Intelligent Technology and Its Applications (ISITIA)*, pages 285–291, 2020.

[5] G. Babiel. *Elektrische Antriebe in der Fahrzeugtechnik: Lehr- und Arbeitsbuch*. Springer Vieweg, 3 edition, 2020.

[6] U. C. Cabuk, M. Tosun, O. Dagdeviren, and Y. Ozturk. Modeling energy consumption of small drones for swarm missions. *IEEE Transactions on Intelligent Transportation Systems*, 2024.

[7] G. Cai, B.M. Chen, and T.H. Lee. *Unmanned Rotorcraft Systems*. Springer London, 2011.

[8] R. D'Andrea. Guest editorial can drones deliver? *IEEE Transactions on Automation Science and Engineering*, 11(3): 647–648, 2014.

[9] C. Di Franco and G. Buttazzo. Energy-aware coverage path planning of uavs. In *2015 IEEE International Conference on Autonomous Robot Systems and Competitions*, pages 111–117, 2015.

[10] H. Elkholy. Dynamic modeling and control of a quadrotor using linear and nonlinear approaches. Master's thesis, American University in Cairo, 2014.

[11] B. C. Florea and D. D. Taralunga. Blockchain iot for smart electric vehicles battery management. *Sustainability*, 12(10), 2020.

[12] Y. Fouad, N. Rizoug, O. Bouhali, and M. Hamerlain. Optimization of energy consumption for quadrotor uav. In *International Micro Air Vehicle Conference and Flight Competition (IMAV)*, 2017.

[13] P. C. Garcia, R. Lozano, and A. E. Dzul. *Modelling and Control of Mini-Flying Machines*. Springer London, 2005.

[14] S. Gasche, C. Kallies, A. Himmel, and R. Findeisen. Energy aware and safe path planning for unmanned aircraft systems. *arXiv.org*, 2025. (preprint).

[15] G. Hattenberger, M. Bronz, and J. Condomines. Evaluation of drag coefficient for a quadrotor model. *International Journal of Micro Air Vehicles*, 15, 2023.

[16] H. He, R. Xiong, and J. Fan. Evaluation of lithium-ion battery equivalent circuit models for state of charge estimation by an experimental approach. *Energies*, 4:582–598, 2011.

[17] A. Hussein and I. Batarseh. An overview of generic battery models. In *2011 IEEE Power and Energy Society General Meeting*, pages 1–6, 2011.

[18] N. Kazantzis, K. T. Chong, J. H. Park, and Alexander G. Parlos. Control-Relevant Discretization of Nonlinear Systems With Time-Delay Using Taylor-Lie Series. *Journal of Dynamic Systems, Measurement, and Control*, 127(1):153–159, 04 2004.

[19] Z. Kingston, M. Moll, and L. E. Kavraki. Sampling-based methods for motion planning with constraints. *Annual review of control, robotics, and autonomous systems*, 1(1):159–185, 2018.

[20] J. Kuffner and S. LaValle. Rrt-connect: An efficient approach to single-query path planning. In *Proceedings 2000 ICRA. Millennium Conference. IEEE International Conference on Robotics and Automation. Symposia Proceedings*, volume 2, pages 995–1001, 2000.

[21] M. Li, G. Jia, S. Gong, and R. Guo. Energy consumption model of bldc quadrotor uavs for mobile communication trajectory planning. *IEEE Wireless Communications Letters*, 2022.

[22] I. Lovas and M. Andras. Quadcopter power consumption analyzation at different landing trajectories. In *2018 IEEE 18th International Symposium on Computational Intelligence and Informatics (CINTI)*, pages 217–222, 2018.

[23] T. T. Mac, Copot C., D. T. Tran, and R. De Keyser. Heuristic approaches in robot path planning: A survey. *Robotics and Autonomous Systems*, 86:13–28, 2016.

[24] D. Malyuta, T. P. Reynolds, M. Szmuk, T. Lew, R. Bonalli, M. Pavone, and B. Açıkmeşe. Convex optimization for trajectory generation: A tutorial on generating dynamically feasible trajectories reliably and efficiently. *IEEE Control Systems Magazine*, 42(5):40–113, 2022.

[25] N. Michel, A. Sinha, Z. Kong, and X. Lin. Multiphysical modeling of energy dynamics for multirotor unmanned aerial vehicles. In *2019 International Conference on Unmanned Aircraft Systems*, pages 738–747, 2019.

[26] S. A. H. Mohsan, N. Q. H. Othman, Y. Li, M. H. Alsharif, and M. A. Khan. Unmanned aerial vehicles (uavs): practical aspects, applications, open challenges, security issues, and future trends. *Intelligent Service Robotics*, 16(1):109–137, 2023.

[27] F. Morbidi, R. Cano, and D. Lara. Minimum-energy path generation for a quadrotor uav. In *2016 IEEE International Conference on Robotics and Automation (ICRA)*, pages 1492–1498, 2016.

[28] C. Muli, S. Park, and M. Liu. A comparative study on energy consumption models for drones. In *Internet of Things*, pages 199–210. Springer International Publishing, 2022.

[29] A. Nagaty, S. Saeedi, C. Thibault, M. Seto, and H. Li. Control and navigation framework for quadrotor helicopters. *Journal of Intelligent & Robotic Systems*, 70:1–12, 2013.

[30] A. Nikolian, J. de Hoog, K. Fleurbaey, J.-M. Timmermans, O. Noshin, P. Van den Bossche, and J. Van Mierlo. Classification of electric modeling and characterization methods of lithium-ion batteries for vehicle applications. In *European Electric Vehicle Congress*, pages 1–15, 2014.

[31] K. Nonami, F. Kendoul, S. Suzuki, W. Wang, and D. Nakazawa. *Autonomous Flying Robots: Unmanned Aerial Vehicles and Micro Aerial Vehicles*. Springer Japan, 2010.

[32] N. Osmić, M. Kurić, and I. Petrović. Detailed octorotor modeling and pd control. In *2016 IEEE International Conference on Systems, Man, and Cybernetics (SMC)*, pages 2182–2189, 2016.

[33] B.K. Patle, G. Babu L, A. Pandey, D.R.K. Parhi, and A. Jagadeesh. A review: On path planning strategies for navigation of mobile robot. *Defence Technology*, 15(4):582–606, 2019.

[34] Pixhawk, 01.07.2023. URL https://pixhawk.org.

[35] R. Quirynen and S. Safaoui, S.and Di Cairano. Real-time mixed-integer quadratic programming for vehicle decision-making and motion planning. *IEEE Transactions on Control Systems Technology*, PP:1, 01 2024.

[36] G. Singhal, B. S. Bansod, and L. Mathew. Unmanned aerial vehicle classification, applications and challenges: A review. *Preprints*, November 2018.

[37] J. K. Stolaroff, C. Samaras, E. R. O'Neill, A. Lubers, A. S. Mitchell, and D. Ceperley. Energy use and life cycle greenhouse gas emissions of drones for commercial package delivery. *Nature Communications*, 9:2041–1723, 2018.

[38] The MathWorks Inc. MATLAB version: R2023a, 2023. URL https://www.mathworks.com.

[39] B. Theys and J. De Schutter. Forward flight tests of a quadcopter unmanned aerial vehicle with various spherical body diameters. *International Journal of Micro Air Vehicles*, 12, 2020.

[40] B. G. van der Wall. *Grundlagen der Hubschrauber-Aerodynamik*. Springer-Verlag, 2020.

[41] J. Vivia, E. Prataviera, N. Gastaldello, and A. Zarrella. A comparison between grey-box models and neural networks for indoor air temperature prediction in buildings. *Journal of Building Engineering*, 84:108583, 2024.

[42] P. Wang, Z. Man, Z. Cao, J. Zheng, and Y. Zhao. Dynamics modelling and linear control of quadcopter. In *2016 International Conference on Advanced Mechatronic Systems (ICAMechS)*, pages 498–503, 2016.

[43] H. Wei and Y. Shi. Mpc-based motion planning and control enables smarter and safer autonomous marine vehicles: Perspectives and a tutorial survey. *IEEE/CAA Journal of Automatica Sinica*, 09 2022.

[44] D. Yang, Y. Liu, Q. Chen, M. Chen, S. Zhan, N. Cheung, H. Chan, Z. Wang, and W. Li. Development of the high angular resolution 360° lidar based on scanning mems mirror. *Scientific Reports*, 13(1540), 2023.

[45] J. Zhang, J. Campbell, D. Sweeney, and A. Hupman. Energy consumption models for delivery drones: A comparison and assessment. *Transportation Research Part D: Transport and Environment*, 90:102668, 2021.

[46] W. Zhou, Y. Zheng, Z. Pan, and Q. Lu. Review on the battery model and soc estimation method. *Processes*, 9, 2021.